Fuel 427 (2027) 139808

Contents lists available at ScienceDirect

Fuel

journal homepage: www.elsevier.com/locate/fuel

Full Length Article

Enhanced hydrogen separation through H_2-Selective PMMA/CAU-1 thin film nanocomposite membrane

Nur Amalina Shairah Abdul Samat [a,b], Pei Sean Goh [a,d,*], Woei Jye Lau [a], Guo Qingjie [c,d], Guo Tuo [d], Ahmad Fauzi Ismail [a]

[a] Advanced Membrane Technology Research Centre (AMTEC), Universiti Teknologi Malaysia (UTM), Skudai, Johor 81310, Malaysia
[b] Department of Chemical Engineering and Energy Sustainability, Faculty of Engineering, Universiti Malaysia Sarawak (UNIMAS), Kota Samarahan, Sarawak 94300, Malaysia
[c] College of Chemical Engineering, Qingdao University of Science and Technology, Qingdao 266042, China
[d] Center of Carbon Capture and Industrial Utilization, Jiangmen Laboratory of Carbon Science and Technology, Jiangmen 529020, China

ARTICLE INFO

Keywords:
Metal-organic framework
Christian-Albrechts-University-1 (CAU-1)
polymethyl methacrylate (PMMA)
Hydrogen-selective separation
Thin-film nanocomposite

ABSTRACT

The amine-functionalized Christian-Albrechts-University-1 (CAU-1) metal–organic framework (MOF) possesses intrinsic structural features ideally suited for hydrogen (H_2) separation, with pore apertures closely matching the molecular size of hydrogen, thereby enabling selective hydrogen transport via molecular sieving. The physicochemical and structural tailoring of CAU-1 holds immense potential for gas separation thin-film nanocomposite (TFN) membranes yet it remains largely unexplored. This work presents the first systematic investigation of CAU-1 incorporation confined within a thin PMMA selective layer supported on a polysulfone (PSF) substrate, elucidating its influence on the interfacial structure, gas transport pathways, and hydrogen separation performance of polymethyl methacrylate (PMMA)/CAU-1 TFN membranes. Morphological analyses revealed the successful formation of thin, dense, and defect-free TFN exhibiting excellent polymer-filler compatibility with no observable interfacial voids, while thermogravimetric analysis demonstrated excellent thermal stability up to 360 °C. The optimized PMMA/CAU0.5 membrane achieved an H_2 permeability of 294.43 Barrer, with ideal selectivities of 4.91, 6.30 and 5.03 against carbon dioxide (CO_2), nitrogen (N_2), and methane (CH_4), respectively, representing respective improvements of 11%, 42%, and 51% over pristine PMMA. Under mixed-gas conditions, the H_2/CO_2 separation factor surpassed the Robeson upper limit indicating the effective H_2-selective transport properties. These findings highlight the pivotal role of CAU-1 in creating microporous, H_2-selective transport pathways, demonstrating the potential of PMMA/CAU-1 TFN membranes for enhanced hydrogen purification.

1. Introduction

Membrane technology has gained significant attention as a promising method for hydrogen (H_2) separation due to its energy efficiency, low energy consumption, ease of operation, scalability, and environmental benefits [1,2]. Its effectiveness is primarily governed by permeability and selectivity, which are intrinsically influenced by the physical and chemical properties of the materials used [3]. Recent advancements in nanomaterials have shown to enhance the performance of nanoporous membranes, revolutionizing the field of gas separation.

Metal-organic frameworks (MOFs) have attracted increasing attention as advanced materials in membrane development owing to their tunable porosity, high surface area, and excellent chemical and thermal stability. By tailoring their metal nodes and organic linkers, MOFs allow precise control over pore size, shape, and topology, enabling effective molecular sieving and gas transport [4]. Moreover, chemical functionalization and activation can further enhance their interaction with the target gases, thereby improving their separation performance. Various MOF-based membranes, such as those incorporating ZIF-7 [4–7], ZIF-8 [8–12], MIL-53 [13–15], and UiO-66 [16–19], have been widely explored for hydrogen purification, exhibiting moderately promising separation performance.

Recent studies on MOF-based nanocomposite membranes highlighted both the potential and limitations of these membranes for hydrogen separation. Shahbaz et al. [20] synthesized amino-functionalized bimetallic Zn/Co-ZIF-NH_2 in 6FDA-DAM MMMs,

* Corresponding author.
E-mail address: peisean@petroleum.utm.my (P.S. Goh).

https://doi.org/10.1016/j.fuel.2026.139808
Received 22 January 2026; Received in revised form 4 May 2026; Accepted 6 May 2026
Available online 15 May 2026
0016-2361/© 2026 Elsevier Ltd. All rights are reserved, including those for text and data mining, AI training, and similar technologies.

achieving very high H_2 permeability (3273 Barrer) at 35 °C and 2 bar but negligible H_2/carbon dioxide (CO_2) selectivity (~1). Similarly, Sun et al. [21] reported high H_2 permeability (1128 Barrer) with high H_2/nitrogen (N_2) and H_2/methane (CH_4) selectivities (28.2 and 23) for their UiO-66-Br/Tröger's base MMMs under comparable conditions; however, H_2/CO_2 selectivity remained low (1.48), indicating limited molecular sieving for CO_2. Meanwhile, Friebe et al. [18] observed moderate H_2/CO_2 and H_2/N_2 selectivities (~5) alongside extremely high H_2 permeability in UiO-66/Matrimid TFNs under ambient conditions. In contrast, Xiang et al. [22] achieved an opposite trend for ultrathin UiO-66 TFNs, exhibiting high H_2/CO_2 selectivity (20.3) but very low permeability (1.2 Barrer), thereby illustrating the inherent permeability-selectivity trade-off. Zhao et al. [13] further showed that ultrathin CAU-1-NH_2/PI and MIL-53-NH_2/PMMA MMMs could reach high H_2/CO_2 selectivities (32.8 and 53.1) at 2 bar and room temperature, but at the expense of low H_2 permeability (~28 and 10 Barrer). Overall, these studies highlight the intrinsic limitations of existing MOF-based nanocomposites, where simultaneously achieving high permeability and selectivity remains challenging.

Christian-Albrechts-University-1 (CAU-1) MOF features a pore aperture of 0.38 nm, which closely matches the molecular diameter of hydrogen (0.29 nm), thereby suggesting strong potential for selective hydrogen transport via molecular sieving mechanism [23]. Its three-dimensional microporous network, constructed from aluminum-oxygen (Al-O) clusters and 2-amino-1,4-benzenedicarboxylic acid (H_2N-H_2BDC) linkers, comprises distorted octahedral and tetrahedral cages with effective diameters of approximately 1.0 and 0.45 nm, respectively [24]. In addition, its exceptional chemical, mechanical, and thermal stability under high-pressure and high-temperature conditions positions CAU-1 as a promising MOF candidate for advanced hydrogen separation membranes. Despite extensive investigations on various MOFs, limited attention has been directed toward CAU-1 as functional fillers in hydrogen (H_2)-selective membranes. While CAU-1 has been extensively investigated for adsorption [25–28], water purification [29–31], sensor applications [32,33], and non-hydrogen gas separations [34–36], its potential for hydrogen separation remains largely unexplored.

Glassy polymers like polyimides (PI) [13], polybenzimidazoles (PBI) [7,10,37–39], and poly(methyl methacrylate) (PMMA) [13,40,41] have shown effective for H_2-selective separation. PMMA, in particular, demonstrates robust mechanical strength, thermal stability, and excellent processability [42], making it an attractive material for durable, high-performance thin-film membranes. Governed by the solution-diffusion mechanism, PMMA membranes efficiently facilitate the transport and diffusion of small gas molecules such as H_2 and helium (He), while restricting larger species like CO_2, CH_4, and N_2 [43,44]. Its intrinsic chemical compatibility and stability further ensure reliable performance under mixed-gas conditions, reinforcing its suitability for hydrogen purification. Through thermal and mechanical analyses, our previous work confirmed the robustness and suitability of PMMA thin-film composite (TFC) membranes for high-temperature and high-pressure applications [45]. Our optimized PMMA membrane exhibited high H_2 permeability and selectivity toward CO_2, N_2, and CH_4. These findings establish PMMA as a promising matrix for further advancement into thin-film nanocomposite (TFN) membranes, through the incorporation of functional fillers such as CAU-1 MOF, to refine molecular sieving characteristics and achieve superior H_2-selective separation performance.

Incorporating MOFs as fillers in mixed-matrix membranes (MMMs) harnesses the synergistic hybrid effects of the polymer matrix and the MOF, pairing the flexibility and processability of polymers with the precise molecular sieving and tunable properties of MOFs. Despite substantial progress in MOF-based MMMs, persistent challenges continue to limit their scalability and practical implementation. One of the most significant issues is the poor MOF-polymer interfacial adhesion, which often leads to non-selective voids and filler agglomeration within the polymer matrix, thereby compromising selectivity, performance consistency, and reproducibility [46–50]. High MOF loadings, while beneficial for improving gas diffusivity and selective permeability, frequently induce structural defects and mechanical fragility, causing MMMs to become brittle and prone to cracking during operation [51,52]. Moreover, standalone MMMs often exhibit insufficient mechanical integrity under pressurized conditions, thereby limiting their scalability and industrial applicability despite their promising gas separation performance [53]. Consistent with this, our previous work [45] demonstrated that unsupported PMMA membranes were highly susceptible to rupture under abrupt pressure changes and prolonged testing, underscoring the fragility of standalone configurations and their unsuitability for high-pressure gas separation. These findings collectively highlight the need to develop TFN structures capable of minimizing diffusion resistance while maintaining high selectivity and structural stability under pressurized conditions.

To address the inherent limitations of MMMs, this work pioneers the development and systematic investigation of a H_2-selective PMMA/CAU-1 TFN membrane for hydrogen separation from CO_2, N_2 and CH_4 under both pure and mixed-gas conditions. To date, no study has comprehensively examined the H_2 permeability-selectivity behavior of PMMA/CAU-1 within a thin-film configuration, leaving its potential in hydrogen purification largely unexplored. While retaining the synergistic advantages of polymer-MOF hybridization characteristic of MMMs, the TFN architecture enables the formation of a thin selective layer that minimizes diffusion resistance while leveraging the substrate's mechanical support to enhance structural stability and operational durability. Benchmarking against other MOF-based MMMs demonstrates that the developed PMMA/CAU-1 TFNs exhibit competitive H_2 permeability-selectivity performance, indicating their potential for H_2-selective separation.

2. Materials and Methods

2.1. Materials

Polysulfone (PSF) ultrafiltration flat sheet membrane (US020, molecular weight cut-off (MWCO) = 20 kDa, flux rate = 280 L/(m^2.h) at 25 °C, 0.35 MPa), with a non-woven fabric layer, was procured from RisingSun Membrane Technology, China, and served as the substrate for the TFN membranes. PMMA pellets were obtained from Chimei, Taiwan, while acetone solvent (C_3H_6O, 99%) was supplied by Merck. Aluminium chloride hexahydrate ($AlCl_3{\cdot}6H_2O$, >99%), 2-aminoterephthalic acid (H_2N-H_2BDC, >99%), and methanol (CH_3OH, >99%) were also procured from Merck for the synthesis of CAU-1 MOF nanocrystals. All chemicals and reagents of analytical grade were commercially available and used as received. Pure gases (H_2, CO_2, N_2 and CH_4) and binary gas mixtures (H_2/CO_2 and H_2/CH_4, ~50:50) were acquired from Alpha Gas Solutions (AGS) Sdn. Bhd, Malaysia.

2.2. Synthesis of amine-functionalized CAU-1 MOF

CAU-1 MOF powder was synthesized via a solvothermal reaction adapted from previous studies [24,25,27,28]. As outlined in Fig. 1(a), a mixture of $AlCl_3{\cdot}6H_2O$ (10 g, 38.4 mmol) and H_2N-H_2BDC (2.5 g, 12.9 mmol) was suspended in CH_3OH (130 ml) and stirred for one hour or until completely dissolved, maintaining a molar ratio of $AlCl_3{\cdot}6H_2O$: H_2N-H_2BDC at 3:1. The solution was then transferred to a 250 ml Teflon-lined stainless-steel autoclave and heated to 125 °C for 5 h. Upon natural cooling to room temperature, the yellow CAU-1 nanocrystals were collected and subjected to repetitive purification process. The product was centrifuged and washed thoroughly with CH_3OH four times to remove unreacted H_2N-H_2BDC, before further purified in deionized water (250 ml per gram of CAU-1) under continuous stirring overnight to ensure complete removal of chloride ions and other guest impurities in the channel. The purified product was finally recovered through

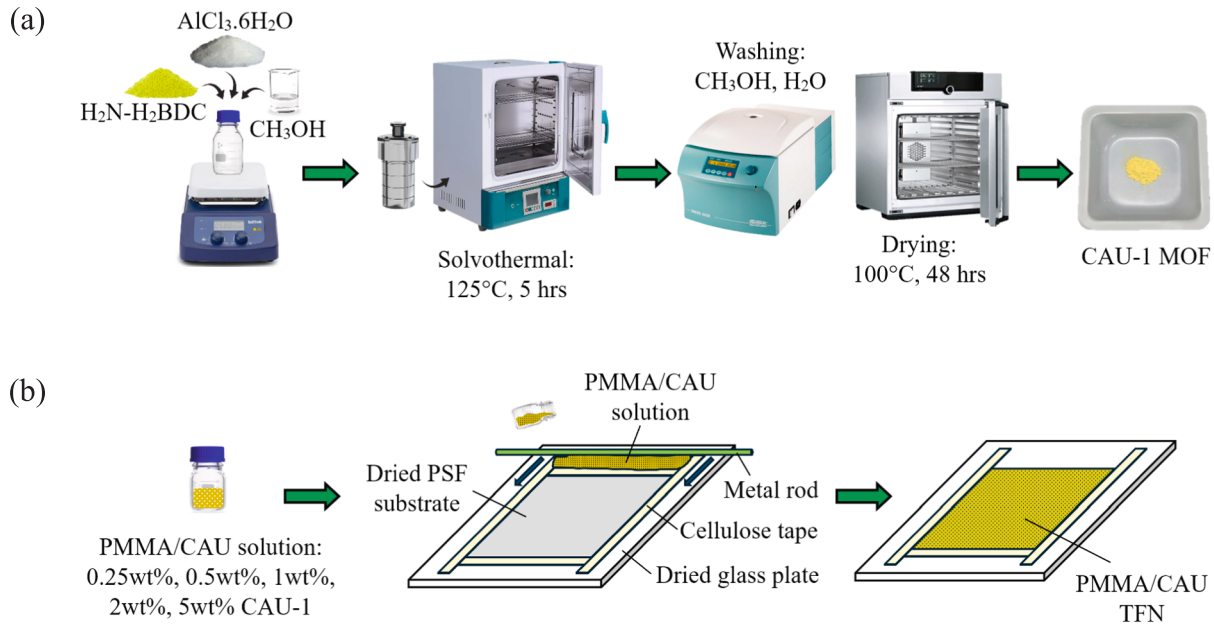


Fig. 1. (a) Synthesis of CAU-1 MOF and (b) fabrication of PMMA/CAU TFN membrane.

centrifugation, dried in a vacuum oven at 100 °C for 48 h, and stored in a vacuum desiccator until further use.

2.3. Membrane preparation and fabrication

1 g of dried PMMA pellets and 0.05 g of synthesized CAU-1 MOF were dispersed in 9 g of acetone to prepare a composite solution with a MOF loading of 0.5 wt% relative to the total PMMA-acetone weight. The PMMA/acetone content was fixed at the optimal concentration of 10 wt % PMMA, as determined in our previous study [45], while the MOF loading was systematically varied from 0.25 to 5 wt%, as detailed in Table 1. The mixture was stirred at 250 rpm at room temperature for a minimum of 6 h, or until complete dissolution of the PMMA pellets was achieved. This was followed by 30 min of sonication to ensure uniform dispersion of the MOF particles, prior to use.

A dry PSF flat-sheet substrate was secured onto a dry glass plate using cellulose tape. To fabricate a thin-film nanocomposite layer, the PMMA/CAU solution was cast onto the PSF substrate using a roll-coating solvent evaporation technique, as illustrated in Fig. 1(b). The membrane was left to dry overnight under ambient conditions, allowing complete evaporation of the acetone solvent.

2.4. Characterization

The structural, morphological, and thermal properties of the synthesized CAU-1 MOF and PMMA/CAU TFN membranes synthesized in this work were comprehensively analyzed. Field emission scanning electron microscopy (FESEM) (Zeiss Crossbeam340) and high-resolution transmission electron microscopy (HR-TEM 120 kV) (Hitachi HT7700) were utilized to examine the morphology and particle size of the synthesized CAU-1 MOF at varying magnifications. Particle size analyzer (PSA) (Malvern Zetasizer Nano ZSP) provides precise nanoparticle size measurements to further validate these findings. Additionally, both FESEM and HRTEM were also employed to investigate the surface and cross-sectional morphologies of the TFN membranes, with magnifications of × 5 k and × 15 k for surface analysis and × 3 k for cross-sectional analysis. Elemental mapping using energy dispersive X-ray spectroscopy (EDX) confirmed the distribution of components within the composite structure.

Atomic force microscopy (AFM) (Park System XE-100), operated in non-contact mode (NC-AFM) with scanning area of 10 μm x 10 μm, was used to analyze the surface topography of the TFN membranes at nanometer-scale resolution, offering insights into surface roughness, uniformity, and the presence of defects. The pore characteristics of both CAU-1 MOF and PMMA/CAU TFN membranes were determined via Brunauer-Emmett-Teller (BET) analysis (Micromeritics Tristar II) using N_2 adsorption–desorption isotherms. Fourier transform infrared spectroscopy (FTIR) (Perkin Elmer Frontier) was conducted to identify functional groups, confirming the chemical integrity of the synthesized CAU-1 MOF and its successful integration into the PMMA matrix. The crystalline structures of both CAU-1 MOF and the TFN membranes were characterized using X-ray diffraction (XRD) analysis (Panalytical X'pert^3 Powder), enabling the assessment of crystallinity and material purity. Thermogravimetric analysis (TGA) (Rigaku STA8122) was used to evaluate the thermal stability of the MOF and membranes over a temperature range of 30 °C to 900 °C, at a heating rate of 10 °C/min. This analysis provides insights into the decomposition profiles and overall thermal robustness of the materials.

Table 1
CAU-1 loading in PMMA-based TFN membranes.

Membrane type	CAU-1 loading (wt%)
PMMA	0
PMMA/CAU0.25	0.25
PMMA/CAU0.5	0.5
PMMA/CAU1	1
PMMA/CAU2	2
PMMA/CAU5	5

2.5. Gas separation test and measurements

Gas separation experiments were conducted at 25 °C using a circular stainless-steel membrane cell with an effective permeation area of 19.6 cm^2. Tests were performed under both pure and mixed gas environments. Feed gas with a constant pressure of 4 bar was introduced into the permeation cell followed by stabilization. In pure gas experiments, the gases were analysed in the sequence of H_2, N_2, CH_4 and CO_2. Upon reaching steady-state conditions, the permeate volumetric flow rate was measured for five independent membrane samples using a digital flowmeter. For mixed gas analysis, the permeate gas was collected in a

leak-proof aluminum gas sampling bag, and their compositions were analyzed using gas chromatography equipped with a thermal conductivity detector (GC-TCD) (Shimadzu GC-2014).

In gas separation processes, permeability and selectivity are critical performance parameters. Gas permeability quantifies the ability of gas molecules to pass through a membrane, reflecting their mobility within the material. Meanwhile, gas selectivity assesses the membrane's separation efficiency, representing its relative capability to preferentially separate specific gases from a gas mixture. Together, these parameters define the efficiency and functionality of a membrane in separation applications.

Gas permeability, P, (in Barrer) [1 Barrer = 1 x 10^{-10} cm^3(STP).cm/(cm^2.s.cmHg)] of pure gases were determined using Eq. (1):

$$P_i = \frac{Q_i L}{A_{eff} \cdot \Delta p_i} \tag{1}$$

where Q_i is the volumetric flow rate of gas component i at standard temperature and pressure (cm^3STP/s), L is the average membrane thickness (cm), A_{eff} is the effective gas permeation area of the membrane (cm^2), and Δp_i is the *trans*-membrane pressure difference of component i (cmHg). The average membrane thickness, L, determined from the FESEM cross-sectional images, considers only the thickness of the selective PMMA/CAU layer, which serves as the primary functional layer for hydrogen separation. The PSF substrate layer was excluded from the thickness measurement, as it has negligible impact on gas separation, owing to its large pore volume relative to the gas molecular dimensions.

The ideal gas selectivity in a pure gas system, expressed as the permeability ratio of the pure gas pair i and j, and the actual separation factor in a mixed gas system, defined as the composition ratio of permeate to feed gas, were determined using Eq. (2) and Eq. (3), respectively.

$$\alpha_j^i = \frac{P_i}{P_j} \tag{2}$$

$$\alpha_j^i = \frac{y_i / y_j}{x_i / x_j} \tag{3}$$

where x_i and y_i are the molar fractions of gas i on the feed and permeate sides respectively.

3. Results and Discussion

3.1. Characterization of CAU-1 MOF

The morphology and size of the synthesized CAU-1 nanoparticles were analyzed using FESEM and HRTEM at different magnifications, as illustrated in Fig. 2(a-b). The bulk nanocrystals exhibits elliptical structures with smooth surfaces and uniform particle diameters ranging from 200 to 300 nm, consistent with previous findings [27,29]. The modal particle size of the CAU-1 MOF, depicted in Fig. 2(c), was determined to be 244.5 ± 54.47 nm, while the N_2 adsorption–desorption isotherm at 77 K, presented in Fig. 2(d), exhibits a characteristic Type I curve without hysteresis, confirming its microporous nature (<2 nm), a highly uniform pore structure, and the absence of significant mesoporous defects or structural irregularities [54]. BET analysis of the synthesized MOF shows a high surface area (S_{BET}) of 1348 m^2g^{-1}, with micropore and Density Functional Theory (DFT) pore volumes of 0.486 cm^3g^{-1} and 0.490 cm^3g^{-1}, respectively, indicating

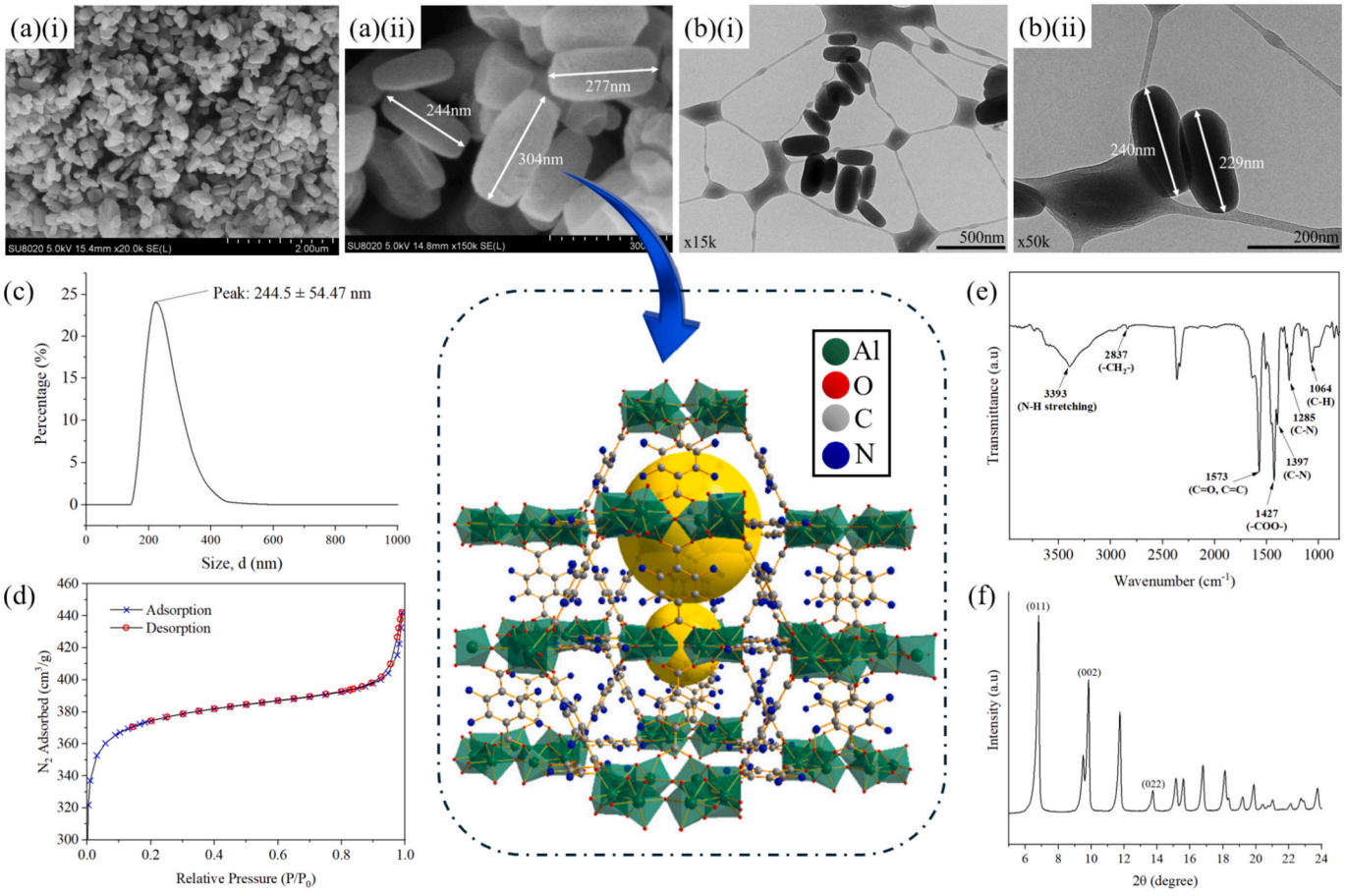


Fig. 2. Characterization of synthesized CAU-1 MOF nanocrystals: (a) FESEM micrograph; (b) HRTEM micrograph; (c) particle size distribution curve; (d) N_2 adsorption–desorption isotherm at 77 K; (e) FTIR spectrum; and (f) XRD diffractogram.

substantial microporosity. These results aligned with the reported ranges of 900 – 1600 m^2g^{-1} (S_{BET}) and 0.4 – 0.6 cm^3g^{-1} (micropore volume) in previous studies [13,24,26,31,36,40,55].

The FTIR spectrum of CAU-1 MOF, presented in Fig. 2(e), closely

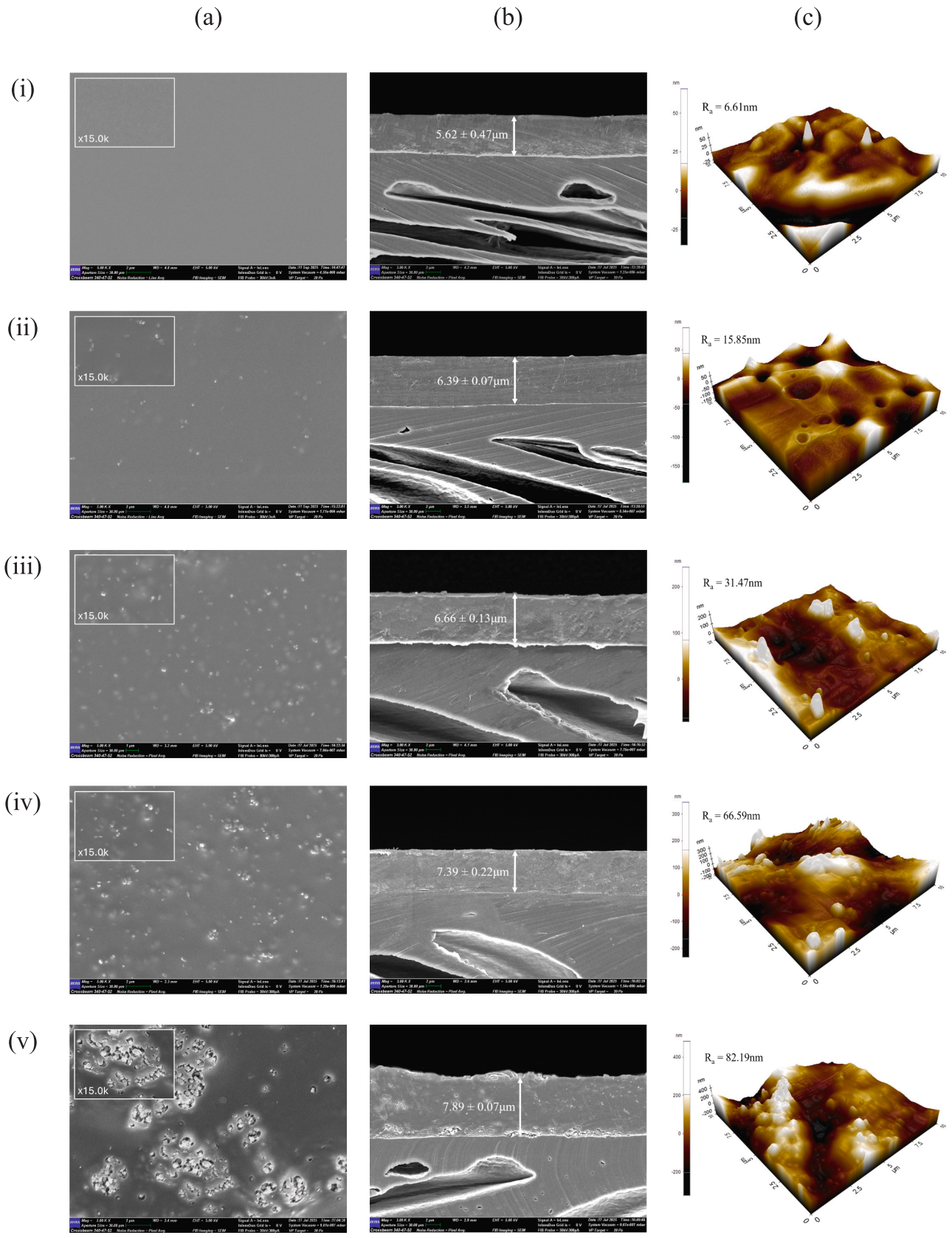


Fig. 3. (a) FESEM surface images, (b) FESEM cross-sectional images, and (c) AFM topography of PMMA/CAU TFNs: (i) PMMA, (ii) PMMA/CAU0.25, (iii) PMMA/CAU0.5, (iv) PMMA/CAU1, (v) PMMA/CAU2, and (vi) PMMA/CAU5.

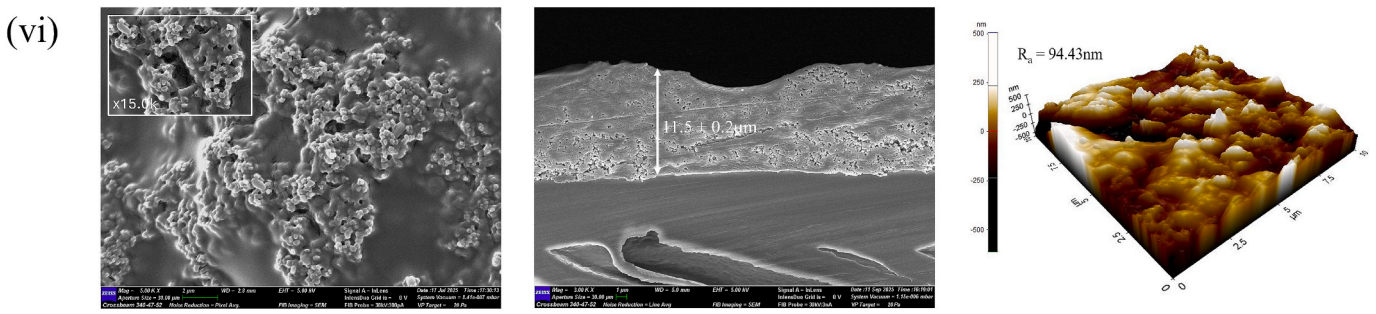


Fig. 3. (*continued*).

aligns with the findings reported by Ahnfeldt et al. [24]. A distinct peak at 3393 cm^{-1} is attributed to the symmetric N–H stretching vibration of amino (–NH_2) groups, while absorption bands in the range of 1285 – 1397 cm^{-1} correspond to the C-N aromatic stretching vibration from the amine-functionalized organic linker, consistent with observations by Xiao et al. [30] and Gumber et al. [28]. These bands confirm the presence of –NH_2 groups in CAU-1 framework [13,27,29], highlighting the presence of amine functionalities that enhance compatibility with PMMA. Absorption peaks at 1573 – 1577 cm^{-1} evidence the presence of the carbonyl (C=O) and C=C stretching vibrations associated with the benzene ring of the CAU-1 MOF [13]. Furthermore, the bridging carboxylate group (–COO^-), derived from the organic linker, is characterized by distinctive peaks in the range of 1600 – 1400 cm^{-1} [30,31], with a prominent peak observed at 1427 cm^{-1} in this study. Gumber et al. [28] identified the asymmetric and symmetric stretching vibrations of these carboxylate groups at 1600 cm^{-1} and 1430 cm^{-1}, respectively, confirming their coordination with the aluminium ion (Al^{3+}) metal centres.

The crystalline structure of the synthesized CAU-1 MOF nanocrystals is studied by XRD, as exhibited in Fig. 2(f). The characteristics peaks at $2\theta = 6.8°$ and 13.7°, corresponding to the (011) and (022) reflections, respectively, confirm the successful synthesis of CAU-1 MOF, aligning with findings from previous studies [24,40]. This result further indicates that the pore size and geometry of the synthesized MOF are comparable to those reported by other researchers. Additionally, a strong peak at $2\theta = 9.8°$, attributed to (002) reflection, suggests the additional attachment of hydroxyl (–OH) functional groups on the CAU-1 crystal surface [27,56]. The seed MOF crystals are observed to be pure, free from impurities, and exhibit high crystallinity.

3.2. Characterization of PMMA/CAU TFN membrane

3.2.1. Morphological analysis

The surface morphologies of PMMA/CAU membranes, presented in Fig. 3(a), reveal that at low CAU-1 loadings (0.25–0.5 wt%), the membrane surfaces are smooth and free from visible cracks, voids, or other defects. The CAU-1 crystals appear uniformly dispersed and well-embedded within the PMMA matrix, with no interfacial voids observed. This uniform integration is attributed to good polymer-filler interfacial adhesion arising from hydrogen bonding between the amine groups of CAU-1 and the carbonyl groups of PMMA, resulting in a compatible and well-integrated interface [13]. At a moderate loading of 1 wt%, small clusters of CAU-1 begin to appear, yet they remain well-incorporated within the matrix without notable agglomeration or surface void formation.

In contrast, higher CAU-1 loadings (2–5 wt%) result in pronounced particle aggregation and uneven dispersion within the selective layer. Beyond the ~ 2 wt% critical threshold, the polymer chains are unable to effectively encapsulate the MOF particles, leading to poor polymer-filler contact, weakened interfacial bonding, and consequently, suboptimal membrane surface formation [57]. This agglomeration is driven by hydrogen bonding between the amine groups on the organic linker and hydroxyl groups in the aluminium-oxygen-aluminium (Al-O-Al) secondary building units of the MOF framework [58].

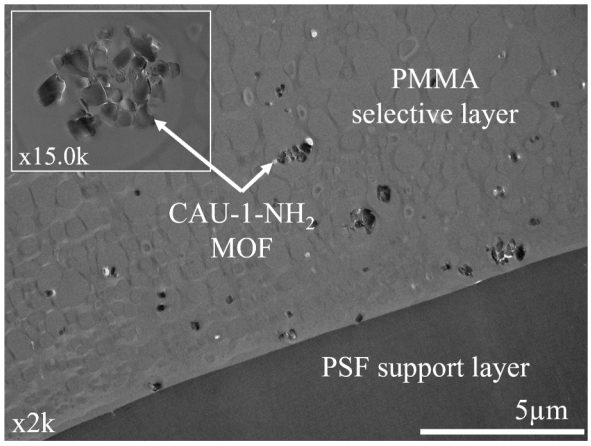
Cross-sectional FESEM images in Fig. 3(b) and the HRTEM image of PMMA/CAU0.5 TFN in Fig. 4(a) clearly demonstrate the successful fabrication of thin TFN membranes. The thin selective layer facilitates reduced gas flow resistance, thereby enhancing permeability [13]. At low MOF loadings, the TFN membranes exhibit smooth, defect-free morphologies, with the selective layer thickness increasing progressively from ~ 5.6 μm (PMMA TFC) to ~ 11.5 μm (PMMA/CAU5) as CAU-1 content increases. This is primarily attributed to the volumetric contribution of large CAU-1 aggregates within the matrix and the increased viscosity of the casting solution at high filler content, which reduces its mobility during membrane formation [13]. These findings highlight that optimizing CAU-1 loading is essential to achieve a good nanomaterial distribution, hence striking a good balance among the desired physicochemical properties in terms of membrane morphology and selective layer thickness. This further ensures strong interfacial adhesion, uniform structure, minimal defects, and ultimately maximizes the gas separation performance of PMMA/CAU TFN membranes.

Fig. 4(b) presents the EDX elemental composition and mapping of PMMA/CAU TFN membranes. Carbon content decreases from 75.4% in the pristine PMMA membrane to 63.6% at the highest CAU-1 loading (PMMA/CAU5), while aluminium, absent in PMMA, appears at 0.2% in PMMA/CAU0.25 and increases steadily to 1.7% in PMMA/CAU5. This inverse C-Al trend reflects the systematic replacement of the carbon-rich PMMA matrix by CAU-1 particles, whose framework contains Al and O, thereby confirming progressive MOF incorporation with increasing loading.

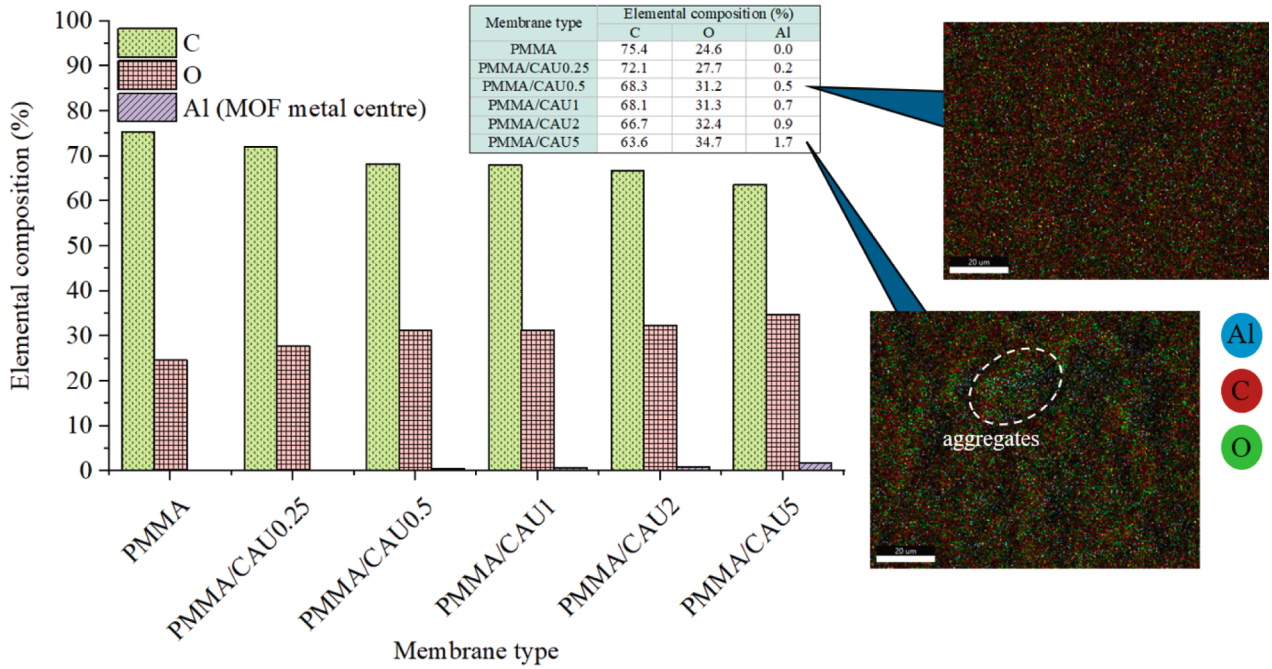
Elemental mapping offers complementary insights into the distribution and dispersion of CAU-1. The C, O, and Al signals in PMMA/CAU0.5 membrane are uniformly distributed, indicating homogeneous MOF dispersion without visible aggregation. In contrast, the PMMA/CAU5 TFN exhibits pronounced particle clustering and large aggregates, in agreement with FESEM observations. These results suggest that at low-to-moderate loadings (≤0.5 wt%), CAU-1 particles are well integrated into the PMMA matrix, maintaining strong polymer–filler interfacial contact.

3.2.2. Surface topology

AFM analysis was conducted to examine changes in the membrane's surface roughness following MOF incorporation. The AFM images in Fig. 3(c) indicate that the pristine PMMA TFC membrane exhibits a much smoother surface compared to the TFN membranes, primarily due to the absence of CAU-1 MOF fillers. A progressive increase in surface roughness (R_a) is then observed with increasing CAU-1 loading from 15.85 nm in PMMA/CAU0.25 TFN to 94.43 nm in PMMA/CAU5 TFN. The smooth thin selective layer with moderate R_a in low MOF content TFNs results from the uniform dispersion of CAU-1 particles within the PMMA matrix, while higher loadings induce particle agglomeration and uneven volume distribution, as evidenced by the FESEM images (Fig. 3 (a)), yielding a rougher surface. This agglomeration disrupts membrane homogeneity by weakening CAU-1-PMMA interactions, thereby



(a)



Membrane type	Elemental composition (%)		
	C	O	Al
PMMA	75.4	24.6	0.0
PMMA/CAU0.25	72.1	27.7	0.2
PMMA/CAU0.5	68.3	31.2	0.5
PMMA/CAU1	68.1	31.3	0.7
PMMA/CAU2	66.7	32.4	0.9
PMMA/CAU5	63.6	34.7	1.7

(b)

Fig. 4. (a) HRTEM cross-section morphology of PMMA/CAU0.5 TFN and (b) EDX elemental composition and mapping of PMMA TFC and PMMA/CAU TFNs.

hindering uniform particle dispersion and causing surface irregularities during film formation. Based on these results, maintaining a low MOF content (≤0.5 wt% CAU-1) is essential to form a smooth, dense surface layer with moderate roughness, which minimizes morphological defects and suppresses non-selective permeation, thus enhancing selectivity for effective hydrogen separation.

3.2.3. *Pore analysis*

BET analysis was performed to assess the pore volume variations of PMMA/CAU TFNs. As presented in Fig. 5, the incorporation of CAU-1 MOF into the PMMA matrix markedly increases the pore volumes, owing to the intrinsic microporosity of CAU-1, which contributes additional selective pores within the membrane structure. At low CAU-1 loadings (≤0.5 wt%), the pore volumes remain moderate, indicating that the intrinsic porosity of CAU-1 is well preserved, thereby maintaining micropore accessibility for effective H_2-selective diffusion. In contrary, the significant pore volume observed in TFNs with higher MOF loading, particularly at 5 wt%, is attributed to the formation of aggregation-induced voids, as evinced by the FESEM image in Fig. 3(a)(vi).

3.2.4. *Chemical and functional group analysis*

The FTIR spectra, shown in Fig. 6, reveal the key peaks of the functional groups in the synthesized CAU-1 MOF, PMMA TFC, and PMMA/CAU TFN membranes fabricated with varying MOF loadings. The characteristic amine stretching band of CAU-1 at 3393 cm^{-1} is not clearly discernible in the TFN spectra due to its overlapping with the O–H stretching band spanning between 3200 and 3600 cm^{-1} [28,31].

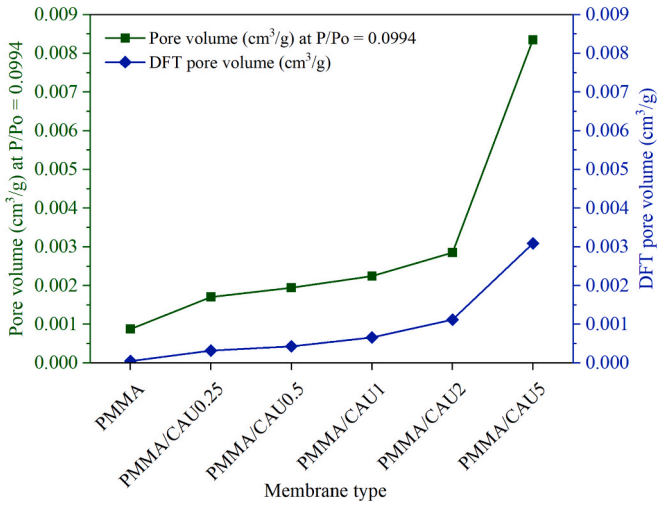


Fig. 5. Pore volumes of PMMA/CAU TFNs.

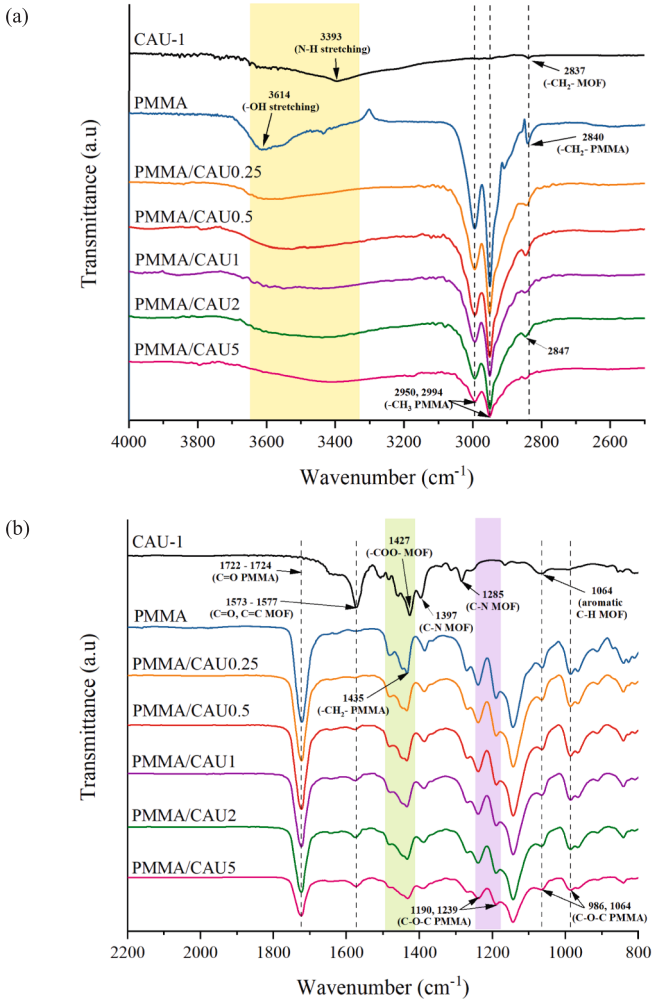


Fig. 6. FTIR spectra of CAU-1 MOF, PMMA TFC and PMMA/CAU TFN membranes in (a) 2600 – 4000 cm^{-1} and (b) 800 – 2200 cm^{-1} wavenumber regions.

The N–H peaks in the TFN spectra exhibit slight shifts, suggesting hydrogen bonding interactions between the MOF and polymer at the interface, which enhance polymer-filler compatibility and promote the formation of a compact selective layer, as schematically illustrated in Fig. 7 [13]. The PMMA pristine membrane prominently exhibits a distinct –OH stretching peak at 3614 cm^{-1}, largely attributed to the presence of residual moisture from the membrane fabrication process.

The characteristic peaks appear in the range of 2950 – 2994 cm^{-1} in the PMMA/CAU TFNs are attributed to the symmetric and asymmetric C–H stretching vibrations of methyl ($–CH_3$) groups of the PMMA polymer matrix [28,42,59–61], while the absorption bands near 2840 cm^{-1} correspond to the symmetric C–H stretching of methylene ($–CH_2$-) groups of both CAU-1 MOF and PMMA [30]. Upon incorporating CAU-1 MOF into PMMA, a slight shift in the symmetric C–H stretching vibration was observed from ~ 2840 cm^{-1} to ~ 2847 cm^{-1}, indicating that PMMA is only minimally influenced by the presence of the MOF [13]. This suggests that the polymer backbone largely retains its original vibrational characteristics, while CAU-1 is primarily dispersed physically within the matrix without forming covalent bonds with the polymer C–H sites. Instead, the MOF-polymer interactions are predominantly governed by hydrogen bonding. Additionally, the intensity of the C–H peaks decreases with increasing MOF content. Higher MOF content disrupts the packing and alignment of the polymer chains, leading to a diminished prominence of $–CH_3$ and $–CH_2$- vibrational modes and a corresponding decrease in their peak intensities.

High intensity peaks observed around 1722 – 1724 cm^{-1} corresponds to the C=O groups of the PMMA structure [42,61]. This peak is absent in CAU-1 MOF but appears in the PMMA/CAU TFN spectra, confirming its origin from the PMMA component. Besides, the intensity of the carboxylate C=O and C=C stretching vibrations of the benzene ring in the CAU-1 MOF, observed at absorption bands 1573 – 1577 cm^{-1} in PMMA/CAU TFNs, increases with higher MOF concentration, implying the successful incorporation of MOF particles into the thin-film composite. Moreover, no significant peak shift is observed in the FTIR spectra upon MOF incorporation, suggesting that no chemical bonding or interaction occurs with the carboxylate groups or the benzene ring of the MOF [13]. This indicates that the structural integrity of the MOF is maintained within the composite. Additionally, the overlap between 1427 cm^{-1} peak (ascribed to the symmetric stretching of $–COO^-$ group in the MOF) [27,30] and 1435 cm^{-1} peak (ascribed to the CH_2 bending vibration in the PMMA backbone or side chains) [61,62] in PMMA/CAU TFNs results in a broadened and reduced absorption (green region), which becomes more pronounced with increasing MOF loading. This indicates the coexistence of PMMA and CAU-1 MOF within the TFN structure.

In addition, the peaks observed around 1386 – 1397 cm^{-1} in all TFN samples are likely attributed to the symmetric bending vibrations of CH_3 groups attached to the polymer backbone [63] and the C-N aromatic stretching vibration of the $–NH_2$ groups [28,30]. These overlapping contributions from both the MOF and PMMA reflect the formation of hydrogen bonding interactions between the amino groups of the CAU-1 particles and the PMMA polymer matrix [13]. Overall, the aforementioned findings confirm the successful synthesis and incorporation of CAU-1 MOF within the PMMA TFN membranes.

3.2.5. *Crystallinity analysis*

Fig. 8 illustrates the XRD patterns of the synthesized CAU-1 MOF and PMMA/CAU TFN membranes at different MOF loadings. The TFN characteristic peaks align with those of pristine CAU-1, confirming preservation of the MOF's crystal structure upon incorporation into PMMA [47]. No significant peak shifts are observed with varying loadings, aside from changes in peak intensity below 12° (inset). Notably, the diffraction peak at $2\theta = 6.8°$ becomes more obvious at higher loadings, appearing only in PMMA/CAU2 (2 wt%) and PMMA/CAU5 (5 wt%) TFNs, indicating successful incorporation of CAU-1 into the polymer matrix [13,36]. This is attributed to the increased electron density contrast resulting from higher MOF content. Similarly, Cao et al. [40] reported that the peak intensity at 5 wt% MOF is indistinct but becomes more pronounced as the loading increases up to 25 wt%. However, excessive MOF incorporation can compromise the structural integrity of

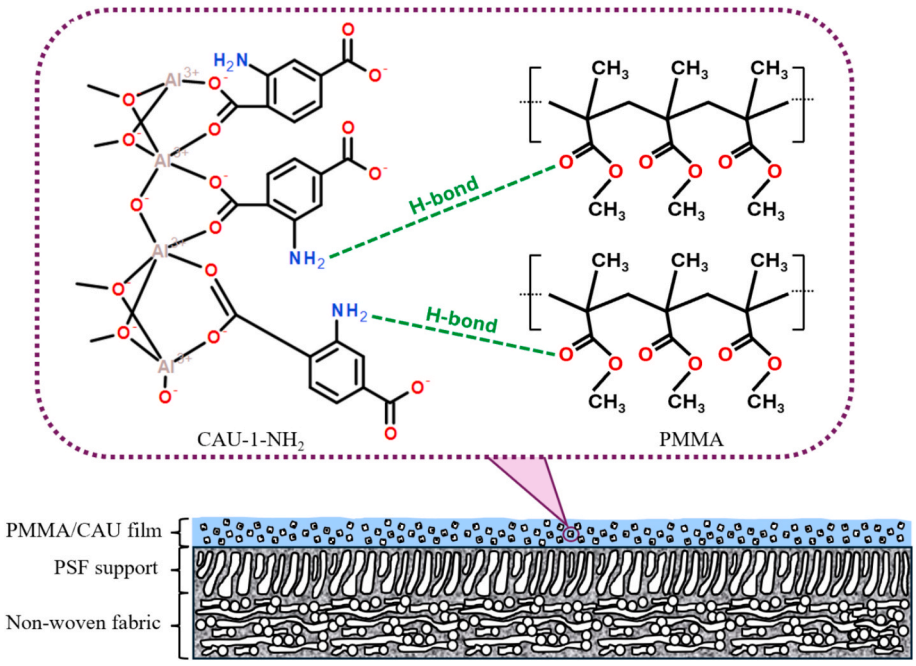


Fig. 7. Schematic illustration of PMMA/CAU TFN membrane and intermolecular hydrogen-bonding interaction between PMMA and amine-functionalized CAU-1 MOF.

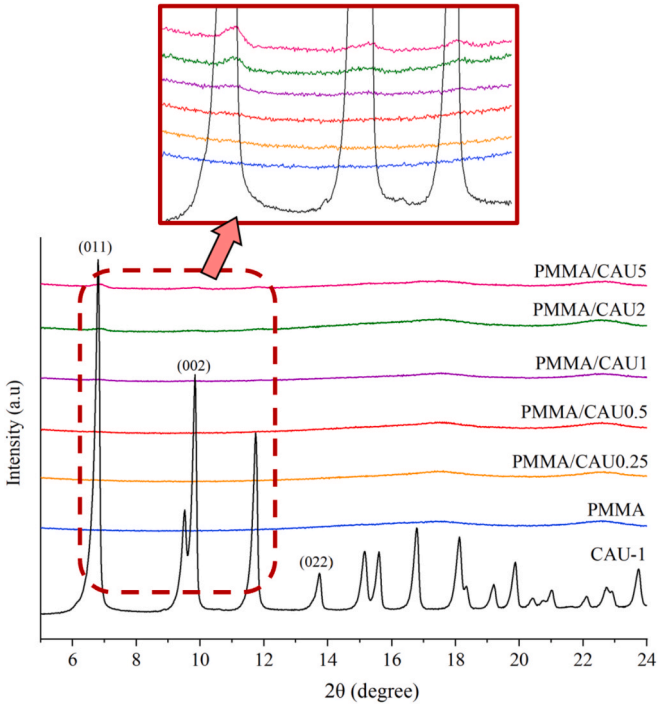


Fig. 8. XRD pattern of CAU-1 MOF, PMMA TFC and PMMA/CAU TFNs.

the TFNs. High crystallinity often reduces flexibility and ductility, making the composite more brittle [64]. These findings highlight the need to maintain an optimal MOF loading that balances crystallinity with mechanical stability, ensuring adequate flexibility and toughness while sustaining high separation performance.

3.2.6. *Thermal stability analysis*

The thermal stability of CAU-1 MOF and PMMA/CAU TFN membranes were evaluated via thermogravimetric analysis over the temperature range of 25 °C to 900 °C, as presented in Fig. 9. The TGA curve of CAU-1 exhibited a distinct two-step weight loss profile. The initial weight loss of approximately 25%, occurring below 100 °C, is attributed to the removal of physisorbed water during dehydration [24,27]. The second stage of weight loss corresponds to the structural collapse of the CAU-1 framework, confirming its thermal stability up to ~ 335 °C, thereby demonstrating its suitability for high-temperature applications. Beyond this point, progressive mass loss is observed, primarily associated with the decomposition of the $H_2BDC\text{-}NH_2$ linker within the framework [27]. These observations are in close agreement with previously reported results [13,26,27,40].

The TGA curves of all PMMA/CAU TFN samples also exhibited a characteristic two-step thermal decomposition profile. The primary decomposition phase, observed between 360 °C and 480 °C, involves a pronounced mass loss of ~ 66–72%, arising from the severe thermal degradation of the PMMA matrix coupled with the structural disintegration of the incorporated MOF nanoparticles [44,65]. This combined decomposition behaviour suggests that the CAU-1 particles were fully

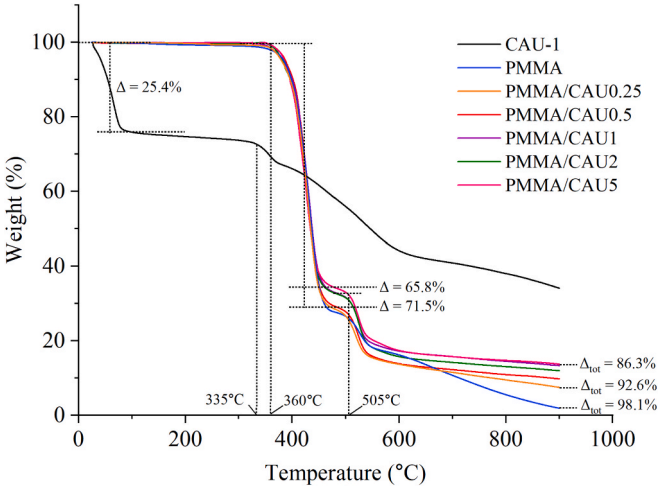


Fig. 9. TGA curves of CAU-1 MOF, PMMA TFC and PMMA/CAU TFNs.

incorporated into the PMMA matrix with strong interfacial bonding, enabling the composite to decompose as a single integrated component rather than as separate phases [66]. The observed degradation temperature (T_d) of 360 °C demonstrates that the prepared TFNs possess superior thermal stability compared to typical MMMs, which generally withstand temperatures of only ~ 300 °C [13,40,44]. This enhanced thermal stability highlights the robust structural integrity of the TFN architecture relative to MMMs, enabling sustained performance under elevated temperatures. This makes it well suited for high-temperature gas separation applications such as hydrogen purification from hot syngas in steam reforming or gasification processes, and pre-combustion CO_2 capture in integrated gasification combined cycle (IGCC) power plants [37,67,68]. The second degradation stage, observed at approximately 505 °C corresponds to further thermal breakdown of residual polymer chains and structural disintegration of CAU-1 MOF framework.

Overall, the similar degradation phases and onset decomposition temperatures observed for the pristine PMMA TFC and PMMA/CAU TFN samples indicate that the incorporation of CAU-1 MOF particles had a negligible effect on the overall thermal stability of the membranes [69]. Although MOF incorporation is commonly reported to restrict polymer chain mobility, thereby delaying the onset of thermal degradation or reducing the degradation rate [58,70], such an effect was not evident in

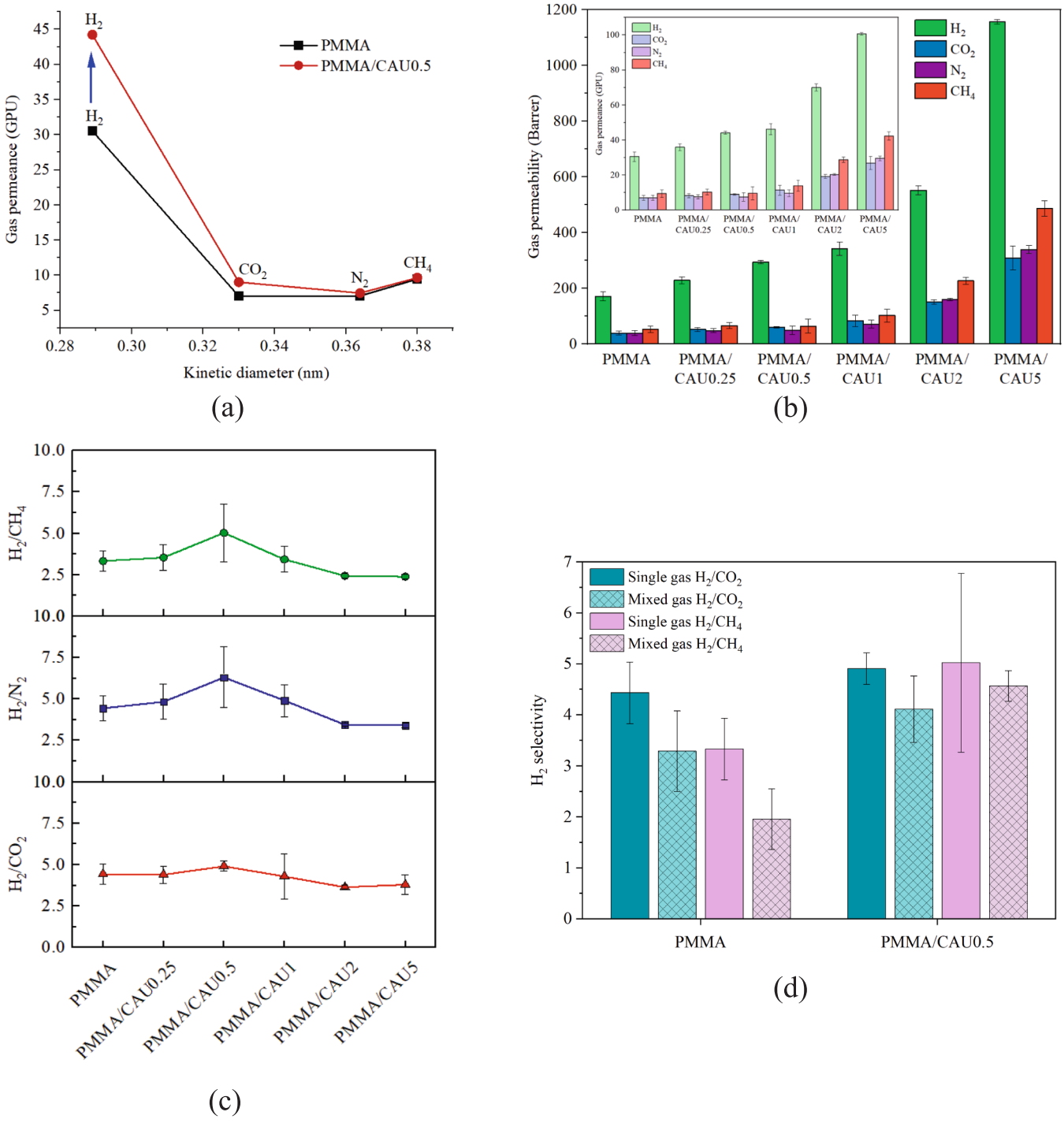


Fig. 10. Gas separation performances of PMMA/CAU TFNs at 25 °C and 4 bar permeation: (a) Gas permeance versus kinetic diameter; (b) Permeability and permeance; (c) Ideal selectivity; and (d) Mixed gas analysis.

this work. In addition, no discernible trend was observed in the effect of CAU-1 MOF loading on the thermal stability of the TFNs, in contrast to the findings reported in previous studies [13,44,65,71]. This minimal impact is likely attributable to the comparatively low MOF content relative to the polymer fraction used in this work, with a maximum variation of 5 wt%, as opposed to studies commonly employing MOF loadings above 10 wt%. Consequently, the thermal stability of the TFNs is predominantly governed by the intrinsic properties of the polymer matrix rather than by minor variations in CAU-1 MOF content. Furthermore, unlike MMMs, which are composed solely of polymer and filler particles, the TFNs developed in this work incorporate a thermally stable PSF substrate, which further minimizes the influence of MOF loading on thermal stability.

It is also noteworthy that the PMMA/CAU TFN samples exhibited markedly lower total weight losses, ranging from 86% to 92%, and consequently higher residual masses compared to the pristine PMMA TFC, which demonstrated a total weight loss of 98%. This improvement is attributed to the inorganic and structurally robust framework of the CAU-1 MOF, confirming the successful incorporation of thermally stable CAU-1 particles within the PMMA matrix. Besides, increasing the MOF content within the membranes corresponds to a greater amount of residues, consistent with previous studies [3,71].

3.3. H_2 gas separation performance

Single and mixed gas permeation tests were performed to evaluate the H_2 separation performance of the prepared PMMA/CAU TFN membranes. In this study, H_2-selective separation is primarily achieved by the thin PMMA/CAU selective layer, while the porous PSF substrate solely provides mechanical support with negligible impact on gas permeation. The negligible contribution of the PSF support to gas separation was validated through a preliminary permeation testing of the pristine PSF substrate without the PMMA selective layer. The substrate exhibited extremely high gas flux with no measurable selectivity among the tested gases, indicating negligible mass transfer resistance due to its highly porous structure. Fig. 10 and Table 2 present the gas separation performance of the prepared TFNs as a function of CAU-1 MOF loading, measured at room temperature under 4 bar single gas conditions.

At 0.5 wt% CAU-1 loading, a marked improvement in both H_2 permeability and the ideal selectivity for H_2/CO_2, H_2/N_2, and H_2/CH_4 gas pairs is observed, relative to the pristine PMMA TFC membrane. H_2 permeability increases evidently by 72% from 171.53 ± 15.96 Barrer (PMMA), while the ideal selectivity for H_2 over CO_2, N_2 and CH_4 improves by 11%, 42% and 51% from 4.43 ± 0.61, 4.44 ± 0.74 and 3.33 ± 0.60, respectively. The simultaneous enhancement in both H_2 permeability and selectivity deviates from the conventional permeability-selectivity trade-off characteristic observed in pure polymer membranes, indicating the formation of microporous, size-selective H_2 transport channels induced by the CAU-1 MOF. This suggests that CAU-1 at the optimal loading establishes highly accessible and effective molecular sieving pathways, resulting in enhanced H_2 separation performance [4,36,40].

The microporous CAU-1 MOF with pore size of ~ 0.38 nm optimally matches the kinetic diameter of H_2 (~0.29 nm), enabling preferential H_2-selective diffusion through the MOF channels. Although CO_2 (~0.33 nm), N_2 (~0.364 nm), and CH_4 (~0.38 nm) are competitively small, H_2 experiences a lower steric resistance than the larger gases under competitive transport conditions. The narrow CAU-1 pore aperture constrains the simultaneous transport of multiple gas species, favouring H_2 permeation to the permeate side while retaining larger gases on the feed side [23]. Fig. 10(a) correlates the gas permeances of H_2, CO_2, N_2, and CH_4 with their kinetic diameters through PMMA TFC and PMMA/CAU0.5 TFN membranes at 25 °C and 4 bar. In both membranes, a steep decline in permeance is observed from H_2 to CO_2, N_2, and CH_4, indicating strong size-dependent transport. For the pristine PMMA TFC membrane, the trend is governed solely by the solution-diffusion mechanism, where smaller H_2 molecules diffuse more readily through the rigid glassy PMMA matrix, while larger gases experience greater diffusional resistance. In contrast, the PMMA/CAU0.5 TFN membrane demonstrates markedly higher H_2 permeance relative to larger gases. Consistent with the relative gas kinetic diameters, this enhancement is attributed to the molecular sieving effect imparted by the CAU-1 framework, as widely reported for MOF-based systems in prior studies [23,72,73]. This effect introduces an additional size-selective transport pathway alongside the PMMA solution-diffusion mechanism. Additionally, the ideal selectivity values surpass the corresponding Knudsen constants of 4.69, 3.74, and 2.83, indicating that the PMMA/CAU0.5 TFN demonstrates suitability for gas separation applications [23]. In essence, the gas transport in PMMA/CAU0.5 TFN membranes is synergistically governed by PMMA solution-diffusion and CAU-1 molecular sieving, with the dominant contribution of the latter evidenced by the simultaneous enhancement of H_2 permeability and selectivity upon MOF incorporation.

Fig. 10(b) illustrates a pronounced increase in gas permeability with

Table 2
Gas separation performances of PMMA/CAU TFNs.

Sample[a]	MOF loading (wt%)	Membrane thickness (μm)	H_2 permeance (GPU)	Permeability, P (Barrer)[b]					Ideal Selectivity / Separation Factor[c], α_j^i	
				P_{H_2}	P_{CO_2}	P_{N_2}	P_{CH_4}	$\alpha_{CO_2}^{H_2}$	$\alpha_{N_2}^{H_2}$	$\alpha_{CH_4}^{H_2}$
PMMA	0	5.62 ± 0.47	30.52 ± 2.84	171.53 ± 15.96	39.43 ± 7.50	39.64 ± 8.42	53.15 ± 12.02	4.43 ± 0.61 3.29 ± 0.79[c]	4.44 ± 0.74 –	3.33 ± 0.60 1.96 ± 0.60[c]
PMMA/CAU0.25	0.25	6.39 ± 0.07	35.91 ± 2.02	229.48 ± 12.91	52.68 ± 7.17	48.57 ± 7.64	66.27 ± 10.35	4.40 ± 0.52	4.84 ± 1.07	3.54 ± 0.78
PMMA/CAU0.5	0.5	6.66 ± 0.13	44.21 ± 0.86	294.43 ± 5.72	60.09 ± 2.74	49.73 ± 15.64	64.23 ± 24.76	4.91 ± 0.31 4.11 ± 0.65[c]	6.30 ± 1.83 –	5.03 ± 1.75 4.57 ± 0.30[c]
PMMA/CAU1	1	7.39 ± 0.22	46.30 ± 3.20	342.19 ± 23.68	83.92 ± 20.14	71.43 ± 13.96	103.08 ± 23.24	4.29 ± 1.37	4.91 ± 0.96	3.43 ± 0.78
PMMA/CAU2	2	7.89 ± 0.07	69.97 ± 2.06	552.06 ± 16.22	151.45 ± 8.49	160.29 ± 3.71	227.47 ± 12.12	3.65 ± 0.10	3.44 ± 0.10	2.43 ± 0.16
PMMA/CAU5	5	11.5 ± 0.20	100.59 ± 074	1156.82 ± 8.45	309.12 ± 43.33	339.30 ± 14.35	486.82 ± 27.60	3.80 ± 0.59	3.41 ± 0.15	2.38 ± 0.16

[a] Tested at room temperature (RT) (25 °C), 4 bar; STP = standard temperature and pressure
[b] 1 Barrer = 1×10^{-10} cm^3 (STP).cm/(cm^2.s.cmHg)
[c] mixed gas environment

increasing CAU-1 MOF loading, which directly correlates with the enhanced pore volume of the TFN membranes observed in Fig. 5. Importantly, H_2 permeance (inset) increases concurrently despite the thicker selective layer evident from the FESEM images in Fig. 3. As permeance is inversely proportional to thickness, the simultaneous increase in both permeability and permeance indicates enhanced H_2 diffusivity imparted by CAU-1, thus confirming that the improvement is intrinsically driven rather than thickness-related. Although CO_2, N_2, and CH_4 permeabilities also increase with increasing MOF loading, their increments remain comparatively modest, with H_2 consistently exhibiting the highest permeability and permeance across all loadings, thereby confirming the preferential hydrogen transport governed by molecular sieving [23]. In addition, since gas permeability is governed by the product of diffusivity and solubility, and H_2 exhibits significantly lower solubility than CO_2, N_2, and CH_4, the observed higher H_2 permeability cannot be attributed to solubility effects. Instead, it reflects diffusivity-dominated transport arising from molecular sieving and the intrinsic microporosity of the MOF nanoparticles [11]. If solubility were dominant, higher permeability would be expected for more condensable gases such as CO_2 and CH_4, which is not observed.

Fig. 11 presents the H_2 adsorption isotherm of CAU-1 MOF at 77 K and the CO_2 adsorption isotherm at 303 K, reported by Cao et al. [40]. The steep Type I H_2 isotherm, characterized by rapid uptake at low pressure and a saturation plateau (~11 mmol g^{-1}), confirms the well-defined microporosity of CAU-1 and the presence of narrow pore environments suitable for size-selective transport. In contrast, CO_2 exhibits a near-linear and low uptake at 303 K, indicating limited sorption-driven selectivity under ambient conditions. Since permeation experiments were conducted at 25 °C, adsorption effects are minimal and diffusion dominates the gas transport [23]. The observed preferential H_2 permeability against other gases is therefore more plausibly attributed to faster diffusion of the smaller H_2 molecule (kinetic diameter 2.89 Å) through the confined micropores, demonstrating diffusion-governed molecular-sieving behaviour rather than adsorption [23].

The hydrogen separation performance of the PMMA/CAU0.5 TFN membrane is anticipated to further improve under elevated temperature conditions. Gas transport in TFN membranes generally follows an Arrhenius-type behaviour, where permeability is governed by the activation energy of permeation. As temperature rises, the kinetic energy of gas molecules increases, accelerating diffusional transport and enhancing permeation rates. H_2, in particular, typically has a lower activation energy than larger gases such as CO_2, N_2, and CH_4 due to its smaller kinetic diameter and weaker sorption interactions. This difference in activation energy preferentially enhances hydrogen transport especially at elevated temperatures, leading to simultaneous increases in both H_2 permeability and selectivity, consistent with observations reported for MOF-based polymeric membranes [5,74].

Uniform dispersion of MOF crystals at optimal loading, along with strong interfacial interactions with the polymer matrix, is also essential for achieving superior membrane performance [40]. This is exemplified by the PMMA/CAU0.5 TFN sample, which demonstrates optimal H_2 separation performance, owing to the well-dispersed CAU-1 MOF within the polymer matrix, as shown in Fig. 4(b). The significant hydrogen bonding between the amino groups of CAU-1 MOF and PMMA, as illustrated in Fig. 7, enhances polymer-filler interaction, forming robust PMMA/CAU selective layer. In addition, the thin architecture of PMMA/CAU membranes also reduces diffusion resistance, enabling faster H_2 transport through the matrix and thereby enhancing H_2 permeance and overall separation efficiency [23,40].

Further increase in CAU-1 loading beyond 0.5 wt% leads to a substantial rise in gas permeabilities, accompanied by a pronounced decline in H_2/CO_2, H_2/N_2, and H_2/CH_4 ideal selectivities, as depicted in Fig. 10 (c). This indicates that the permeability-selectivity trade-off becomes apparent at excessive MOF loadings, negating the molecular sieving effects of CAU-1 MOF. This dramatic change is primarily due to severe CAU-1 agglomeration at high loadings [36], which compromises the integrity of the dense surface layer, as witnessed in the FESEM and AFM images in Fig. 3. Agglomeration disrupts the uniform distribution of CAU-1 particles and creates interfacial voids within the matrix, forming non-selective gas transport pathways that allow undesired gases such as CO_2, N_2 and CH_4 to bypass the intrinsic molecular sieving effect of the MOF-polymer matrix. This leads to gas leakage, ultimately diminishing the selective advantage for H_2 [36,40]. Consequently, the selectivity for H_2/CO_2, H_2/N_2, and H_2/CH_4 falls below that of the pristine membrane, and the separation performance of the TFNs no longer exhibits linear correlation with CAU-1 loading.

These findings highlight the importance of optimizing MOF content in TFN membranes to achieve high gas separation performance. At optimal loading, the molecular sieving effect of MOF is maximized while maintaining a favorable balance between permeability and selectivity.

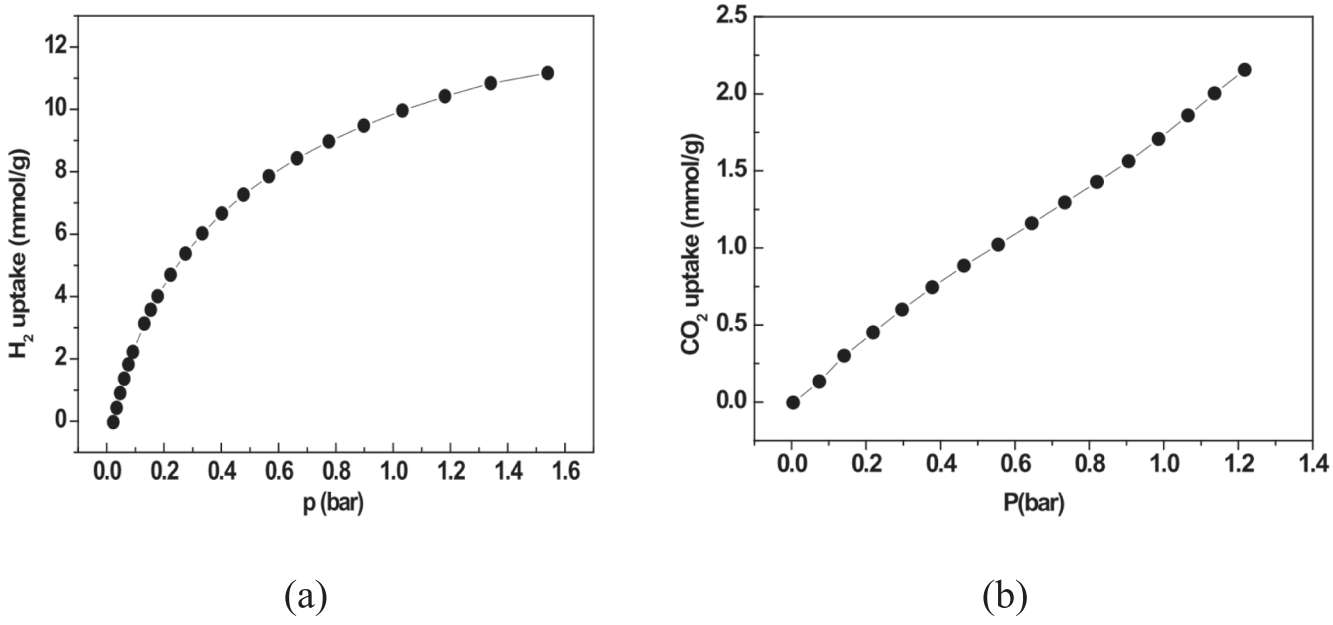


Fig. 11. Adsorption isotherms of CAU-1: (a) H_2 at 77 K and (b) CO_2 at 303 K [40].

In this work, the optimal PMMA/CAU0.5 TFN membrane demonstrated excellent H_2 separation performance, achieving H_2 permeability of 294.43 ± 5.72 Barrer and corresponding H_2/CO_2, H_2/N_2, and H_2/CH_4 ideal selectivity values of 4.91 ± 0.31, 6.30 ± 1.83, and 5.03 ± 1.75, and H_2/CO_2 and H_2/CH_4 separation factors of 4.11 ± 0.65 and 4.57 ± 0.30, respectively. Overall, the separation performances confirm the effectiveness of CAU-1 MOF in enabling H_2-selective separation.

Table 3 benchmarks the hydrogen separation performance of CAU-1-based membranes reported in the literature against the present work, highlighting clear distinctions in both architecture and separation performances. The PMMA/CAU-1 flat-sheet membrane reported by Cao et al. [40] adopted a conventional MMM configuration with a relatively thick selective layer and substantially higher filler loadings. Although higher H_2 permeability was observed, SEM micrographs revealed notable interfacial voids at 5 and 15 wt%, indicating that the permeability enhancement was partially attributed to non-selective defects. At lower loadings, the H_2/CO_2 selectivity remained limited, indicating the reliance of MMM systems on high filler content, which increases the risk of particle agglomeration, defect formation, and overall material cost. Meanwhile, Zhao et al. [13] developed an ultrathin tubular CAU-1/PI membrane supported on a silica-modified ceramic substrate, representing a fundamentally different membrane material and architecture. Despite achieving high H_2/CO_2 selectivity at 20 wt% loading, the membrane exhibited severely compromised H_2 permeability, reflecting diffusion constraints and a pronounced permeability-selectivity trade-off typical of high-loading MMM systems. In contrast, the present work introduces a TFN architecture in which CAU-1 is spatially confined within a thin PMMA selective layer at an ultralow optimal loading of 0.5 wt%. The polymer-filler interfacial compatibility effectively suppresses non-selective defect formation while facilitating efficient gas transport pathways, resulting in high H_2 permeability with competitive H_2/CO_2 selectivity without relying on excessive filler incorporation. Achieving balanced separation performance with minimal MOF consumption evidences the significance of thin-film nanoconfinement as a more material-efficient and structurally optimized alternative to conventional MMM designs.

3.4. Performance benchmarking and future direction

Fig. 12 presents the H_2/CO_2 permeability-selectivity performance of the PMMA/CAU TFN membranes developed in this work, benchmarked against a range of reported MMMs on Robeson's plot. Although the Robeson upper bounds are formally defined for dense, self-supporting polymer membranes, the comparative evaluation is performed as a reference to contextualize the relative performance of the developed PMMA-based TFN membranes amongst other polymer membranes. Notably, all TFNs surpass the 2008 Robeson upper bound (highlighted in blue), underscoring their potential for H_2 purification. Among the fabricated membranes, PMMA/CAU5 demonstrates the highest H_2 permeability, while PMMA/CAU0.5 achieves the most favorable permeability-selectivity balance, delivering superior H_2/CO_2 selectivity while maintaining appreciable H_2 permeability. Such performance highlights the effectiveness of rational MOF incorporation in tailoring membrane transport properties.

When compared with other MOF-based MMMs, the TFN membranes developed in this work demonstrate a distinctly competitive performance profile. Table 4 summarizes the H_2/CO_2 separation performance of MOF-based MMMs reported from the literature, noting that these values were obtained under varying operating conditions, including differences in pressure, temperature, membrane thickness, and MOF loading. Although direct comparison may not be entirely equitable due to these variations, MMMs incorporating fillers such as MIL-53 [13], CAU-1 [40], ZIF-90 [75], ZIF-7 [7], and ZIF-8 [11] generally exhibited higher H_2/CO_2 selectivity but suffer from significantly lower H_2 permeability. In contrast, the PMMA/CAU TFNs exhibit enhanced permeability, albeit with moderately lower selectivity, reflecting the inherent permeability-selectivity trade-off commonly observed in membrane development. Notably, PMMA/CAU0.5 surpasses the selectivity performance reported by Li et al. [76] while maintaining comparable permeability, thus highlighting the effectiveness of optimized MOF loading.

Several reported MMMs incorporating ZIFs [7,12,76], UiO-66 [57], palladium (Pd) [39], and graphene oxide (GO) [41] remain below the Robeson upper bound, indicating their limited separation efficiency relative to the TFNs. The ability of the PMMA/CAU TFNs to outperform these systems confirms their competitive advantage and suggests their potential as practical H_2-selective membranes. Conversely, exceptional performances were achieved by Sánchez-Láinez et al. [77] and Ma et al. [5] using ZIF-based MMMs at elevated operating temperatures (≥100 °C). Their results emphasize the favorable influence of high temperature on gas transport, where H_2 permeability increases significantly due to its low diffusion activation energy, while CO_2 permeability is less affected or even reduced due to diminished CO_2 sorption [37]. This divergence leads to a marked improvement in H_2/CO_2 selectivity, consistent with the thermally activated diffusion mechanism.

Beyond surpassing Robeson's bounds, the mechanical robustness of the TFN configuration provides an additional benefit over conventional MMMs, making them more suited for high-pressure H_2 separation processes [45]. This combination of high permeability, favorable selectivity, and improved structural integrity positions PMMA/CAU TFNs as a more feasible and industrially relevant alternative to standalone MMMs for H_2 separation.

Future research on PMMA/CAU TFN membranes should investigate their performance under industrially relevant operating conditions, such as elevated temperatures and pressures, while exploring targeted modifications to further enhance their stability, permeability, and selectivity. Potential strategies include surface functionalization of CAU-1 to improve polymer compatibility, incorporation of metal nanoparticles such as Pd or nickel (Ni) to promote hydrogen adsorption and diffusion, and post-synthetic modification of the MOF framework to fine-tune pore size and chemical affinity. This scope will be covered in our future study. Collectively, these approaches could advance PMMA/CAU TFN membranes toward reliable, high-performance hydrogen separation, paving the way for their large-scale implementation in industrial applications.

4. Conclusion

This study demonstrates the successful development and optimization of thin PMMA/CAU-1 TFN membranes for efficient H_2-selective separation, featuring smooth, defect-free selective layers with uniformly dispersed CAU-1 crystals firmly integrated within the PMMA matrix. The membranes exhibit excellent thermal stability up to 360 °C, underscoring their robustness for high-temperature gas separation. At the optimal of 0.5 wt% CAU-1 loading, the PMMA/CAU0.5 membrane

Table 3
Comparison of H_2 separation performances of CAU-1-based membranes.

Polymer	Configuration	Thickness (μm)	Loading (wt%)	Operating condition	H_2 permeability (Barrer)	H_2/CO_2 selectivity	Ref.
PMMA	Flat sheet MMM	10	5	RT, 3 bar	5×10^3	3.5	[40]
			15		1.1×10^4	13	
PI	Tubular MMM	0.3	20	RT, 2 bar	27	32.8	[13]
PMMA	Flat sheet TFN	6.66	0.5	RT, 4 bar	294.43 ± 5.72	4.91 ± 0.31	This work

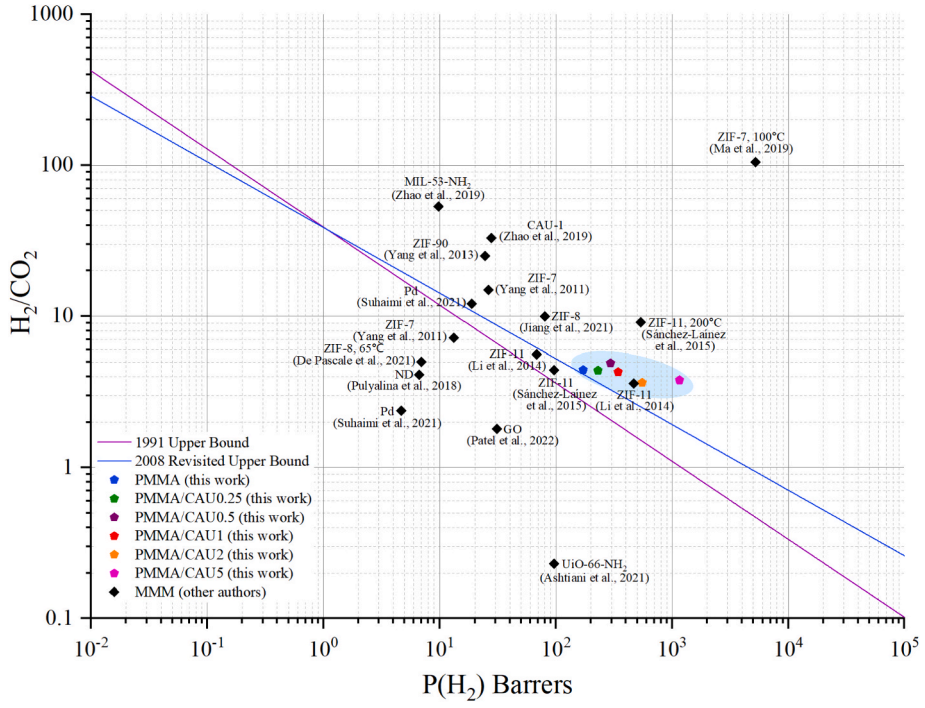


Fig. 12. H_2/CO_2 separation performance of PMMA/CAU TFNs benchmarked against other reported MMMs on Robeson's plot.

Table 4
H_2/CO_2 separation performances of MOF-based MMMs.

Polymer	Filler	Thickness (μm)	Loading (wt%)	Operating condition	H_2 permeability (Barrer)	H_2/CO_2 selectivity	Ref.
PMMA	MIL-53-NH_2	0.3	20	RT, 2 bar	21.5	44.6	[13]
PI	CAU-1	0.3	20	RT, 2 bar	27.6	32.8	
PMMA	CAU-1	10	15	RT, 3 bar	1.1 x 10^4	13	[40]
PBI	ZIF-90	–	45	35 °C, 3.5 atm	24.5	25	[75]
PBI	ZIF-7	–	50	35 °C, 3.5 atm	26.2	14.9	[7]
PI	ZIF-7	5	50	100 °C, 2 bar	5,227	104.8	[5]
Matrimid	ZIF-8	–	20	35 °C, 3.5 atm	~75	<5	[78]
Torlon	ZIF-8	64.7	6	65 °C, 1.3 bar	7	5	[12]
PBI	ZIF-11	–	16	RT, N/A	67.8	5.6	[76]
			40		464.7	3.6	
Matrimid	nZIF-11	87	25	35 °C, 330 kPa	95.9	4.4	[77]
			15	200 °C, 330 kPa	535	9.1	
PEI	UiO-66-NH_2	–	23	RT, 1 bar	96	0.23	[57]

exhibited preferential hydrogen permeation with improved separation performance, attributed to the intrinsic microporosity and molecular sieving characteristics of CAU-1 which promote diffusion-selective hydrogen transport. Overall, the results indicate that PMMA/CAU-1 TFN membranes provide a viable approach for enhancing H_2-selective separation, while further evaluation under extended operating environments and industrially relevant conditions is necessary to assess their broader practical applicability.

CRediT authorship contribution statement

Nur Amalina Shairah Abdul Samat: Writing – review & editing, Writing – original draft, Visualization, Validation, Project administration, Methodology, Investigation, Formal analysis, Data curation, Conceptualization. **Pei Sean Goh:** Writing – review & editing, Validation, Supervision, Resources, Funding acquisition, Conceptualization. **Woei Jye Lau:** Writing – review & editing, Supervision. **Guo Qingjie:** Writing – review & editing, Supervision. **Guo Tuo:** Writing – review & editing. **Ahmad Fauzi Ismail:** Writing – review & editing.

Declaration of competing interest

The authors declare that they have no known competing financial interests or personal relationships that could have appeared to influence the work reported in this paper.

Acknowledgements

The authors would like to acknowledge the facility and financial supports provided by Universiti Malaysia Sarawak (UNIMAS), The National Foreign Experts Program of China (H20240298) and Universiti Teknologi Malaysia (UTM).

Data availability

Data will be made available on request.

References

[1] Liu C, Zhang X, Zhai J, Li X, Guo X, He G. Research progress and prospects on hydrogen separation membranes. Clean Energy 2023;7:217–41. https://doi.org/10.1093/ce/zkad014.

[2] Zhao C, Hussain W, Chlib Alkaaby HH, Al-Khafaji RM, Alghazali T, Izzat SE, et al. Polymeric nanocomposite membranes for gas separation: Performance, applications, restrictions and future perspectives, Case Stud. Therm Eng 2022;38:102323. https://doi.org/10.1016/j.csite.2022.102323.

[3] Yousef S, Tuckute S, Tonkonogovas A, Stankevičius A, Mohamed A. Ultra-permeable CNTs/PES membranes with a very low CNTs content and high H2/N2 and CH4/N2 selectivity for clean energy extraction applications. J Mater Res Technol 2021;15:5114–27. https://doi.org/10.1016/j.jmrt.2021.10.125.

[4] Park S, Cho KY, Jeong HK. Polyimide/ZIF-7 Mixed-Matrix Membranes: Understanding in-situ Confined Formation of ZIF-7 Phases inside Polymer and their Effects on Gas Separations. J Mater Chem A 2020;8:11210–7. https://doi.org/10.1039/d0ta02761h.

[5] Ma X, Wu X, Caro J, Huang A. Polymer Composite Membrane with Penetrating ZIF-7 Sheets Displays High Hydrogen Permselectivity, Angew. Chemie 2019;131:16302–6. https://doi.org/10.1002/ange.201911226.

[6] Li Y, Liang F, Bux H, Yang W, Caro J. Zeolitic imidazolate framework ZIF-7 based molecular sieve membrane for hydrogen separation. J Memb Sci 2010;354:48–54. https://doi.org/10.1016/j.memsci.2010.02.074.

[7] Yang T, Xiao Y, Chung TS. Poly-/metal-benzimidazole nano-composite membranes for hydrogen purification. Energy Environ Sci 2011;4:4171–80. https://doi.org/10.1039/c1ee01324f.

[8] Wijenayake SN, Panapitiya NP, Nguyen CN, Huang Y, Balkus KJ, Musselman IH, et al. Composite membranes with a highly selective polymer skin for hydrogen separation. Sep Purif Technol 2014;135:190–8. https://doi.org/10.1016/j.seppur.2014.08.015.

[9] Mirzaei A, Navarchian AH, Tangestaninejad S. Mixed matrix membranes on the basis of Matrimid and palladium-zeolitic imidazolate framework for hydrogen separation. Iran Polym J (English Ed 2020;29:479–91. https://doi.org/10.1007/s13726-020-00812-w.

[10] Yang T, Shi GM, Chung TSC. Symmetric and asymmetric zeolitic imidazolate frameworks (ZIFs)/Polybenzimidazole (PBI) nanocomposite membranes for hydrogen purification at high temperatures. Adv Energy Mater 2012;2:1358–67. https://doi.org/10.1002/aenm.201200200.

[11] Jiang X, He S, Han G, Long J, Li S, Lau CH, et al. Aqueous One-step Modulation for Synthesizing Monodispersed ZIF-8 Nanocrystals for Mixed-Matrix Membrane. ACS Appl Mater Interfaces 2021;13:11296–305. https://doi.org/10.1021/acsami.0c22910.

[12] De Pascale M, Benedetti FM, Lasseuguette E, Ferrari MC, Papchenko K, Esposti MD, et al. Mixed matrix membranes based on Torlon® and ZIF-8 for high-temperature, size-selective gas separations. Membranes (Basel) 2021;11:1–19. https://doi.org/10.3390/membranes11120982.

[13] Zhao Y, Zhao D, Kong C, Zhou F, Jiang T, Chen L. Design of thin and tubular MOFs-polymer mixed matrix membranes for highly selective separation of H2 and CO2. Sep Purif Technol 2019;220:197–205. https://doi.org/10.1016/j.seppur.2019.03.037.

[14] Zhang F, Zou X, Gao X, Fan S, Sun F, Ren H, et al. Hydrogen selective NH2-MIL-53 (Al) MOF membranes with high permeability. Adv Funct Mater 2012;22:3583–90. https://doi.org/10.1002/adfm.201200084.

[15] Li W, Su P, Zhang G, Shen C, Meng Q. Preparation of continuous NH2-MIL-53 membrane on ammoniated polyvinylidene fluoride hollow fiber for efficient H2 purification. J Memb Sci 2015;495:384–91. https://doi.org/10.1016/j.memsci.2015.08.049.

[16] Jia M, Feng Y, Liu S, Qiu J, Yao J. Graphene oxide gas separation membranes intercalated by UiO-66-NH2 with enhanced hydrogen separation performance. J Memb Sci 2017;539:172–7. https://doi.org/10.1016/j.memsci.2017.06.005.

[17] Hu Z, Kang Z, Qian Y, Peng Y, Wang X, Chi C, et al. Mixed Matrix Membranes Containing UiO-66(Hf)-(OH)2 Metal-Organic Framework Nanoparticles for Efficient H2/CO2 Separation. Ind Eng Chem Res 2016;55:7933–40. https://doi.org/10.1021/acs.iecr.5b04568.

[18] Friebe S, Geppert B, Steinbach F, Caro J. Metal-Organic Framework UiO-66 Layer: a Highly Oriented Membrane with Good Selectivity and Hydrogen Permeance. ACS Appl Mater Interfaces 2017;9:12878–85. https://doi.org/10.1021/acsami.7b02105.

[19] Bulanık Durmuş GN, Eren EO, Devrim Y, Colpan CO, Özkan N. High-temperature electrochemical hydrogen separation from reformate gases using PBI/MOF composite membrane. Int J Hydrogen Energy 2023;48:23044–54. https://doi.org/10.1016/j.ijhydene.2023.03.192.

[20] Shahbaz R, Li T, Sun Y, Sharif S, He G, Ma C. Amino-modified bimetallic ZIF (Zn/Co-NH2)/Polyimide-based mixed matrix membranes for enhanced hydrogen separation. Sep Purif Technol 2025;377:134322. https://doi.org/10.1016/j.seppur.2025.134322.

[21] Sun Y, Bi X, Bai L, Li T, Fan F, Gao Z, et al. Mixed matrix membranes incorporating bromine functionalized UiO-66 in the Troger's base polymer for enhanced CO2 capture. Chem Eng Sci 2025;306:121230. https://doi.org/10.1016/j.ces.2025.121230.

[22] Xiang F, Marti AM, Hopkinson DP. Layer-by-layer assembled polymer/MOF membrane for H2/CO2 separation. J Memb Sci 2018;556:146–53. https://doi.org/10.1016/j.memsci.2018.03.081.

[23] Zhou S, Zou X, Sun F, Ren H, Liu J, Zhang F, et al. Development of hydrogen-selective CAU-1 MOF membranes for hydrogen purification by "dual-metal-source" approach. Int J Hydrogen Energy 2013;38:5338–47. https://doi.org/10.1016/j.ijhydene.2013.02.074.

[24] Ahnfeldt T, Guillou N, Gunzelmann D, Margiolaki I, Loiseau T, Ferey G, et al. [Al4(OH)2(OCH3)4(H2N-bdc)3]·xH2O: a 12-Connected Porous Metal-Organic Framework with an Unprecedented Aluminum-Containing Brick. Angew Chem Int Ed 2009;48:5163–6.

[25] Zheng X, Liu S, Rehman S, Li Z, Zhang P. Highly improved adsorption performance of metal-organic frameworks CAU-1 for trace toluene in humid air via sequential internal and external surface modification. Chem Eng J 2020;389:123424. https://doi.org/10.1016/j.cej.2019.123424.

[26] Zhao H, Hou S, Zhao X, Liu D. Adsorption and pH-responsive Release of Tinidazole on Metal-Organic Framework CAU-1. J Chem Eng Data 2019;64:1851–8. https://doi.org/10.1021/acs.jced.9b00106.

[27] Zhong X, Liang W, Wang H, Xue C, Hu B. Aluminum-based metal-organic frameworks (CAU-1) highly efficient UO2 2+ and TcO4- ions immobilization from aqueous solution. J Hazard Mater 2021;407:124729. https://doi.org/10.1016/j.jhazmat.2020.124729.

[28] Gumber N, Pai RV, Bahadur J, Sengupta S, Das D, Goutam UK. γ-Resistant Microporous CAU-1 MOF for Selective Remediation of Thorium. ACS Omega 2023;8:12268–82. https://doi.org/10.1021/acsomega.2c08274.

[29] M.Z.M. Pauzi, N.M. ammar Mahpoz, N. Abdullah, M.A. Rahman, K.H. Abas, A.A. Aziz, M.H. Padzillah, M.H.D. Othman, J. Jaafar, A.F. Ismail, Feasibility study of CAU-1 deposited on alumina hollow fiber for desalination applications, Sep. Purif. Technol. 217 (2019) 247–257. Doi: 10.1016/j.seppur.2019.02.021.

[30] Xiao S, Lu X, Liu H, Gu J, Yu S, Tan X. High-flux nanofiltration membrane with modified highly dispersed MOF particles as nano filler. Water Sci Technol 2022;86:2642–57. https://doi.org/10.2166/wst.2022.357.

[31] Xiao S, Huo X, Fan S, Zhao K, Yu S, Tan X. Design and synthesis of Al-MOF/PPSU mixed matrix membrane with pollution resistance, chinese. J Chem Eng 2021;29:110–20. https://doi.org/10.1016/j.cjche.2020.05.030.

[32] Von Mankowski A, Szendrei-Temesi K, Koschnick C, Lotsch BV. Improving analyte selectivity by post-assembly modification of metal-organic framework based photonic crystal sensors. Nanoscale Horiz 2018;3:383–90. https://doi.org/10.1039/c7nh00209b.

[33] Ming SS, Gowthaman NSK, Lim HN, Arul P, Narayanamoorthi E, Ibrahim I, et al. Aluminium MOF fabricated electrochemical sensor for the ultra-sensitive detection of hydroquinone in water samples. J Electroanal Chem 2021;883:115067. https://doi.org/10.1016/j.jelechem.2021.115067.

[34] Yin H, Wang J, Xie Z, Yang J, Bai J, Lu J, et al. A highly permeable and selective amino-functionalized MOF CAU-1 membrane for CO2–N2 separation. Chem Commun 2014;50:3699–701. https://doi.org/10.1039/c4cc00068d.

[35] Jian Y, Yin H, Chang F, Cheng L, Yang J, Mu W, et al. Facile synthesis of highly permeable CAU-1 tubular membranes for separation of CO2/N2 mixtures. J Memb Sci 2017;522:140–50. https://doi.org/10.1016/j.memsci.2016.08.060.

[36] Guo X, Huang H, Liu D, Zhong C. Improving particle dispersity and CO2 separation performance of amine-functionalized CAU-1 based mixed matrix membranes with polyethyleneimine-grafting modification. Chem Eng Sci 2018;189:277–85. https://doi.org/10.1016/j.ces.2018.06.008.

[37] Yang T, Chung TS. High performance ZIF-8/PBI nano-composite membranes for high temperature hydrogen separation consisting of carbon monoxide and water vapor. Int J Hydrogen Energy 2013;38:229–39. https://doi.org/10.1016/j.ijhydene.2012.10.045.

[38] Giel V, Morávková Z, Peter J, Trchová M. Thermally treated polyaniline/polybenzimidazole blend membranes: Structural changes and gas transport properties. J Memb Sci 2017;537:315–22. https://doi.org/10.1016/j.memsci.2017.04.062.

[39] Suhaimi HSM, Leo CP, Ahmad AL. Hydrogen separation using polybenzimidazole membrane with palladium nanoparticles stabilized by polyvinylpyrrolidone. Int J Energy Res 2021;45:15171–81. https://doi.org/10.1002/er.6793.

[40] Cao L, Tao K, Huang A, Kong C, Chen L. A highly permeable mixed matrix membrane containing CAU-1-NH2 for H2 and CO2 separation. Chem Commun 2013;49:8513–5. https://doi.org/10.1039/c3cc44530e.

[41] Patel HD, Acharya NK. Transport properties of polymer blends and composite membranes for selective permeation of hydrogen. Int J Hydrogen Energy 2022;48:37796–810. https://doi.org/10.1016/j.ijhydene.2022.11.304.

[42] Kathalingam A, Vikraman D, Marimuthu KP, Karuppasamy K, Lee H, Maiyalagan T, et al. Characterization and application of flexible, highly conductive freestanding films of SWCNT and PMMA nanocomposite prepared by facile solution method. Surf Interfaces 2023;40:103161. https://doi.org/10.1016/j.surfin.2023.103161.

[43] Li K, Huang T, Gao Y, Zhou C. Enhancing antioxidant properties of hydrogen storage alloys using PMMA coating. Int J Hydrogen Energy 2023;48:4339–48. https://doi.org/10.1016/j.ijhydene.2022.10.208.

[44] Molavi H, Shojaei A, Mousavi SA. Improving mixed-matrix membrane performance via PMMA grafting from functionalized NH2-UiO-66. J Mater Chem A 2018;6:2775–91. https://doi.org/10.1039/c7ta10480d.

[45] Abdul Samat NAS, Goh PS, Lau WJ, Guo Q, Arthanareeswaran G, Ismail AF. Tailoring the properties and hydrogen separation performance of ultrathin polymethyl methacrylate composite membrane. Int J Hydrogen Energy 113 2025:749–60. https://doi.org/10.1016/j.ijhydene.2025.02.413.

[46] Muthukumaraswamy Rangaraj V, Wahab MA, Reddy KSK, Kakosimos G, Abdalla O, Favvas EP, et al. Metal Organic Framework — based mixed Matrix Membranes for Carbon Dioxide Separation. Recent Advances and Future Directions, Front Chem 2020;8:1–25. https://doi.org/10.3389/fchem.2020.00534.

[47] Venna SR, Lartey M, Li T, Spore A, Kumar S, Nulwala HB, et al. Fabrication of MMMs with improved gas separation properties using externally-functionalized MOF particles. J Mater Chem A 2015;3:5014–22. https://doi.org/10.1039/c4ta05225k.

[48] Wijenayake SN, Panapitiya NP, Versteeg SH, Nguyen CN, Goel S, Balkus KJ, et al. Surface cross-linking of ZIF-8/polyimide mixed matrix membranes (MMMs) for gas separation. Ind Eng Chem Res 2013;52:6991–7001. https://doi.org/10.1021/ie400149e.

[49] Cheng Y, Wang Z, Zhao D. Mixed Matrix Membranes for Natural Gas Upgrading: Current Status and Opportunities. Ind Eng Chem Res 2018;57:4139–69. https://doi.org/10.1021/acs.iecr.7b04796.
[50] Wu X, Liu W, Wu H, Zong X, Yang L, Wu Y, et al. Nanoporous ZIF-67 embedded polymers of intrinsic microporosity membranes with enhanced gas separation performance. J Memb Sci 2018;548:309–18. https://doi.org/10.1016/j.memsci.2017.11.038.
[51] Cheng Y, Datta SJ, Zhou S, Jia J, Shekhah O, Eddaoudi M. Advances in metal-organic framework-based membranes. Chem Soc Rev 2022;51:8300–50. https://doi.org/10.1039/d2cs00031h.
[52] Moreton JC, Denny MS, Cohen SM. High MOF loading in mixed-matrix membranes utilizing styrene/butadiene copolymers. Chem Commun 2016;52:14376–9. https://doi.org/10.1039/c6cc07329h.
[53] Katare A, Kumar S, Kundu S, Sharma S, Kundu LM, Mandal B. Mixed Matrix Membranes for Carbon Capture and Sequestration: challenges and Scope. ACS Omega 2023;8:17511–22. https://doi.org/10.1021/acsomega.3c01666.
[54] Nik OG, Chen XY, Kaliaguine S. Functionalized metal organic framework-polyimide mixed matrix membranes for CO2/CH4 separation. J Memb Sci 2012;413–414:48–61. https://doi.org/10.1016/j.memsci.2012.04.003.
[55] Si X, Jiao C, Li F, Zhang J, Wang S, Liu S, et al. High and selective CO2 uptake, H2 storage and methanol sensing on the amine-decorated 12-connected MOF CAU-1. Energy Environ Sci 2011;4:4522–7. https://doi.org/10.1039/c1ee01380g.
[56] Hinterholzinger F, Scherb C, Ahnfeldt T, Stockb N, Bein T. Oriented growth of the functionalized metal–organic framework CAU-1 on –OH- and –COOH-terminated self-assembled monolayers. PCCP 2010;12:4515–20. https://doi.org/10.1039/c004746p.
[57] Ashtiani S, Khoshnamvand M, Bouša D, Šturala J, Sofer Z, Shaliutina-Kolešová A, et al. Surface and interface engineering in CO2-philic based UiO-66-NH2-PEI mixed matrix membranes via covalently bridging PVP for effective hydrogen purification. Int J Hydrogen Energy 2021;46:5449–58. https://doi.org/10.1016/j.ijhydene.2020.11.081.
[58] Meshkat S, Kaliaguine S, Rodrigue D. Mixed matrix membranes based on amine and non-amine MIL-53(Al) in Pebax® MH-1657 for CO2 separation. Sep Purif Technol 2018;200:177–90. https://doi.org/10.1016/j.seppur.2018.02.038.
[59] Hosseinabadi N. The alkaline-earth metal alanate embedded selective gas permeable PMMA matrix-nanocomposite. Int J Hydrogen Energy 2021;46:2362–75. https://doi.org/10.1016/j.ijhydene.2020.10.125.
[60] Zheng Z, Chen S, Liu X, Wang Y, Bian Y, Feng B, et al. A bioactive polymethylmethacrylate bone cement for prosthesis fixation in osteoporotic hip replacement surgery. Mater Des 2021;209:109966. https://doi.org/10.1016/j.matdes.2021.109966.
[61] Faruq O, Sarkar K, Lee BT. Physicochemical property and cytocompatibility of HyA-PEG loaded PMMA based bone cement. Mater Chem Phys 2023;295:127142. https://doi.org/10.1016/j.matchemphys.2022.127142.
[62] Wong KC, Goh PS, Ng BC, Ismail AF. Thin film nanocomposite embedded with polymethyl methacrylate modified multi-walled carbon nanotubes for CO2 removal. RSC R Soc Chem 2015;5:31683–90. https://doi.org/10.1039/c5ra00039d.
[63] Wang J, Mao Q. Solvent Effects on the thermal and Mechanical Properties of Poly (methyl methacrylate) Casted from Concentrated Solutions. Adv Polym Tech 2011;30:12–20. https://doi.org/10.1002/adv.
[64] Ordoñez MJC, Balkus KJ, Ferraris JP, Musselman IH. Molecular sieving realized with ZIF-8/Matrimid® mixed-matrix membranes. J Memb Sci 2010;361:28–37. https://doi.org/10.1016/j.memsci.2010.06.017.
[65] Hammani S, Barhoum A, Bechelany M, Hammani S, Barhoum A, Bechelany M, et al. Fabrication of PMMA/ZnO nanocomposite : effect of high nanoparticles loading on the optical and thermal properties. J Memb Sci 2017;53:1911–21. https://doi.org/10.1007/s10853-017-1654-9.
[66] Yousef S, Tonkonogovas A, Makarevicius V, Mohamed A. Enhanced gas separation performance for H2 purification using MIL-68(ln)-nh2/PES mixed-matrix membranes. Chemosphere 2024;358:142166. https://doi.org/10.1016/j.chemosphere.2024.142166.
[67] Etxeberria-Benavides M, Johnson T, Cao S, Zornoza B, Coronas J, Sanchez-Lainez J, et al. PBI mixed matrix hollow fiber membrane: Influence of ZIF-8 filler over H2/CO2 separation performance at high temperature and pressure. Sep Purif Technol 2020;237:116347. https://doi.org/10.1016/j.seppur.2019.116347.
[68] Yong WF, Zhang H. Recent advances in polymer blend membranes for gas separation and pervaporation. Prog Mater Sci 2021;116:100713. https://doi.org/10.1016/j.pmatsci.2020.100713.
[69] Dorosti F, Alizadehdakhel A. Fabrication and investigation of PEBAX/Fe-BTC, a high permeable and CO2 selective mixed matrix membrane. Chem Eng Res Des 2018;136:119–28. https://doi.org/10.1016/j.cherd.2018.01.029.
[70] Ehsani A, Pakizeh M. Synthesis, characterization and gas permeation study of ZIF-11/Pebax® 2533 mixed matrix membranes. J Taiwan Inst Chem Eng 2016;66:414–23. https://doi.org/10.1016/j.jtice.2016.07.005.
[71] Hasan MR, Zhao H, Steunou N, Serre C, Malankowska M, Téllez C, et al. Optimization of MIL-178(Fe) and Pebax® 3533 loading in mixed matrix membranes for CO2 capture. Int J Greenh Gas Control 2022;121:103791. https://doi.org/10.1016/j.ijggc.2022.103791.
[72] Jin H, Wollbrink A, Yao R, Li Y, Caro J, Yang W. A novel CAU-10-H MOF membrane for hydrogen separation under hydrothermal conditions. J Memb Sci 2016;513:40–6. https://doi.org/10.1016/j.memsci.2016.04.017.
[73] Li YS, Liang FY, Bux H, Feldhoff A, Yang WS, Caro J. Molecular sieve membrane: Supported metal-organic framework with high hydrogen selectivity. Angew Chemie - Int Ed 2010;49:548–51. https://doi.org/10.1002/anie.200905645.
[74] Sánchez-Laínez J, Zornoza B, Téllez C, Coronas J. On the chemical filler-polymer interaction of nano- and micro-sized ZIF-11 in PBI mixed matrix membranes and their application for H2/CO2 separation. J Mater Chem A 2016;4:14334–41. https://doi.org/10.1039/c6ta06438h.
[75] Yang T, Chung TS. Room-temperature synthesis of ZIF-90 nanocrystals and the derived nano-composite membranes for hydrogen separation. J Mater Chem A 2013;1:6081–90. https://doi.org/10.1039/c3ta10928c.
[76] Li L, Yao J, Wang X, Cheng YB, Wang H. ZIF-11/Polybenzimidazole composite membrane with improved hydrogen separation performance. J Appl Polym Sci 2014;131:1–7. https://doi.org/10.1002/app.41056.
[77] Sánchez-Laínez J, Zornoza B, Mayoral Á, Berenguer-Murcia Á, Cazorla-Amorós D, Téllez C, et al. Beyond the H2/CO2 upper bound: One-step crystallization and separation of nano-sized ZIF-11 by centrifugation and its application in mixed matrix membranes. J Mater Chem A 2015;3:6549–56. https://doi.org/10.1039/c4ta06820c.
[78] Jiang J, Dong Q, McCullough K, Lauterbach J, Li S, Yu M. Novel hollow fiber membrane reactor for high purity H2 generation from thermal catalytic NH3 decomposition. J Memb Sci 2021;629:119281. https://doi.org/10.1016/j.memsci.2021.119281.